Lab on a Chip

CRITICAL REVIEW

Cite this: *Lab Chip*, 2022, **22**, 3987

A review of optoelectrowetting (OEW): from fundamentals to lab-on-a-smartphone (LOS) applications to environmental sensors

Si Kuan Thio [a] and Sung-Yong Park *[b]

Received 24th May 2022,
Accepted 22nd July 2022

DOI: 10.1039/d2lc00372d

rsc.li/loc

Electrowetting-on-dielectric (EWOD) has been extensively explored as an active-type technology for small-scale liquid handling due to its several unique advantages, including no requirement of mechanical components, low power consumption, and rapid response time. However, conventional EWOD devices are often accompanied with complex fabrication processes for patterning and wiring of 2D arrayed electrodes. Furthermore, their sandwich device configuration makes integration with other microfluidic components difficult. More recently, optoelectrowetting (OEW), a light-driven mechanism for effective droplet manipulation, has been proposed as an alternative approach to overcome these issues. By utilizing optical addressing on a photoconductive surface, OEW can dynamically control an electrowetting phenomenon without the need for complex control circuitry on a chip, while providing higher functionality and flexibility. Using commercially available spatial light modulators such as LCD displays and smartphones, millions of optical pixels are readily generated to modulate virtual electrodes for large-scale droplet manipulations in parallel on low-cost OEW devices. The benefits of the OEW mechanism have seen it being variously explored in its potential biological and biochemical applications. This review article presents the fundamentals of OEW, discusses its research progress and limitations, highlights various technological advances and innovations, and finally introduces the emergence of the OEW technology as portable smartphone-integrated environmental sensors.

1. Introduction

Droplet-based microfluidic systems have attracted significant interest for various lab-on-a-chip (LOC) applications in the past decades.[1–4] By manipulating discrete droplets of biological and chemical reagents in an immiscible phase, droplet-based microfluidic devices offer several advantages over single-phase continuous systems, such as rapid mixing, reagent transport without dispersion, and minimization of cross contamination issues between droplets.[5–7] With these benefits, numerous applications have been demonstrated on droplet-based microfluidic devices, including single-cell encapsulation,[8–11] pathogenic bacteria detection[12–14] and polymerase chain reactions (PCRs) for DNA amplification.[15–17] One drawback associated with such droplet-based microfluidic systems is the difficulty in handling individual droplets driven by a continuous oil flow confined along microfluidic channels.[18–20] To overcome this challenging issue, various active-type droplet manipulation mechanisms have been extensively developed, such as dielectrophoresis (DEP),[21–23] electrowetting on dielectric (EWOD),[24–27] thermocapillary force,[28–30] and magnetic force.[31–33]

Among these techniques, EWOD technology has been widely developed for active droplet control. It offers several unique advantages over other active-type mechanisms, including (1) no mechanical components (*e.g.*, pumps or valves) required for fluidic actuation, (2) extremely low power consumption (in the range of ~μW), and (3) rapid response time in milliseconds. A wide range of applications have been demonstrated, including lab-on-a-chip,[34–36] tunable optics,[37–39] thermal cooling of microdevices,[40,41] and energy harvesting[42–46] using EWOD technology. In recent years, many researchers have investigated the optical control of the EWOD mechanism, called optoelectrowetting (OEW) for effective droplet manipulations with the benefits of device simplicity, reconfigurability, flexibility, and functionality.[47–50] Since light can be flexibly patterned and reconfigured on the photoconductive surface of OEW devices, an electrowetting phenomenon can be dynamically controlled without the need for complex control circuitry on a chip typically required for EWOD devices. Using commercially available spatial light modulators such as liquid crystal displays (LCDs), digital micromirror devices (DMDs), and smartphones, millions of

[a] *Department of Mechanical Engineering, National University of Singapore, 9 Engineering Drive 1, 117575, Singapore*
[b] *Department of Mechanical Engineering, San Diego State University, 5500 Campanile Drive, San Diego, CA, 92182, USA. E-mail: spark10@sdsu.edu*

optical pixels are readily generated to modulate virtual electrodes in parallel on low-cost devices. A variety of applications have been involved with the OEW technology, such as droplet dispensing and merging,[51,52] integrated biosensing devices,[53,54] smartphone-based detection of water quality,[55,56] and biochemical and cell analyses.[57,58]

This review paper highlights the technological advances of OEW and its applications as smartphone-integrated biosensors. Since early OEW devices imitated EWOD, the basic concept of the EWOD mechanism is first described in chapter 2. We further discuss about the fundamentals of the OEW technology to explain how an OEW-based droplet actuation principle works differently from the EWOD. Research progress and limitations on different types of OEW technologies and devices are detailed in chapter 3. In chapter 4, further developments and technological innovations in the OEW are presented. Finally, the emergence of the OEW technology as smartphone-integrated portable biosensors is introduced in chapter 5. A brief comparison of these OEW technologies and devices is also summarized in Table 1.

2. Fundamentals of EWOD and OEW

2.1 EWOD-based droplet actuation

Since Lippmann's first study in 1875,[59] electrowetting (EW) has been extensively explored as an effective means for small-scale liquid handling due to the dominance of surface tension forces over body forces on micro-/meso-scales. When an electric potential is applied between a liquid droplet and a solid electrode, the electric charges are re-distributed to modify the surface tension at the liquid–solid interface, where the like-charge repulsion decreases the work by expanding the surface area. The resulting contact angle (θ) of a liquid droplet can be mathematically estimated using the Young–Lippmann equation as follows:[60,61]

Table 1 Table of comparison for various OEW technologies and devices

OEW platform	Droplet size	Light source	Light intensity	Applied voltage & frequency (AC)/electric field (DC)	Active chip area	Actuation speed	Ref.
Early-stage OEW	1.6 μL	Laser (532 nm)	636 mW cm^{-2}	200 V_{pp} 500 Hz	1 cm × 1 cm	7 mm s^{-1}	Chiou *et al.*[47]
Early-stage OEW	0.4 μL	Laser (532 nm)	636 mW cm^{-2}	200 V_{pp} 500 Hz	1 cm × 1 cm	78 mm s^{-1}	Chiou *et al.*[74]
COEW	10–50 pL	HeNe laser (632 nm)	254 W cm^{-2}	200 V_{pp} 10–30 kHz	Not stated	1 mm s^{-1}	Chiou *et al.*[75] Chiou *et al.*[76]
COEW	5 nL–2 μL	Optical projector	1.38 W cm^2	52 V_{pp} 10 kHz	1.5 cm × 1.1 cm	2 cm s^{-1}	Pei *et al.*[78]
COEW + OET	12.5 nL (droplet) 10 μm (beads) HeLa cells	Optical projector	1.38 W cm^{-2}	40 V_{pp}, 10 kHz (OEW) 10 V_{pp}, 200 kHz (OET)	Not stated	8 mm s^{-1} (OEW) 60 μm s^{-1} (OET)	Valley *et al.*[58]
COEW	4 pL	Optical projector	Not stated	188 V_{pp} 500 Hz	Not stated	39 μm s^{-1}	Yu *et al.*[77]
o-OEW	Not stated	Laser (670 nm)	15 mW cm^{-2}	42 V_{rms} 500 Hz	Not stated	3.6 mm s^{-1}	Chuang *et al.*[79]
o-OEW	1 μL	Optical projector	1.5 W cm^{-2}	53 V_{rms} 10 kHz	1 cm × 1.5 cm	4.5 cm s^{-1}	Loo *et al.*[51]
SCOEW	250 pL 0.5 μL 50 μL	Optical projector LCD display	Not stated	Not stated (DC)	5 cm (electrode gap)	102 μm s^{-1} 510 μm s^{-1} 17.5 mm s^{-1}	Park *et al.*[80]
SCOEW	20 μL	Optical projector	1.5 W cm^{-2}	120 V (DC)	5 cm (electrode gap)	12 mm s^{-1}	Shekar *et al.*[52]
SCOEW	8 μL	Optical projector	Not stated	200 V (DC)	2.5 cm (electrode gap)	4.86 mm s^{-1} (y-direction)	Liu *et al.*[81]
Flexible SCOEW	3 μL	Optical projector	13.6 mW cm^{-2}	30 V mm^{-1} (DC)	Not stated	3.3 mm s^{-1}	Jiang *et al.*[50]
Plasmonic-enhanced SCOEW	1 μL	Optical projector	13.6 mW cm^{-2}	100 V mm^{-1} (DC)	2 cm (electrode gap)	12.5 mm s^{-1} (instantaneous speed)	Thio *et al.*[107]
SCOEW	5 μL	Smartphone	140 μW cm^{-2}	35 V mm^{-1} (DC)	2 cm (electrode gap)	2.5 mm s^{-1}	Jiang *et al.*[56]
SCOEW	1 μL	Smartphone	140 μW cm^{-2}	120 V mm^{-1}	2 cm (electrode gap)	2 mm s^{-1}	Lee *et al.*[117]
Plasmonic-enhanced SCOEW	2.5 μL	Smartphone	140 μW cm^{-2}	100 V mm^{-1}	4 cm (electrode gap)	1.21 mm s^{-1}	Thio *et al.*[55]

$$\cos\theta = \cos\theta_0 + \frac{c_d(\Delta V)^2}{2\gamma_{LG}} \quad (1)$$

where θ_0 is the initial contact angle of the droplet with zero potential application, γ_{LG} is the surface tension between two immiscible fluids (*i.e.*, the liquid droplet and its surrounding medium), c_d is the capacitance of a dielectric layer per unit area, and ΔV indicates the voltage drop across a dielectric capacitor.

Conventional EW uses electrolytes in direct contact with a solid electrode, where an electric double layer capacitor (EDLC) is formed to hold the storage energy induced by applying an electric potential. However, the thickness of the EDLC is typically very thin (less than 10 nm), and susceptible to electric breakdown.[61,62] As a result, contact angle modulation of a droplet is seriously limited in conventional EW as the process is irreversible after electric breakdown. Later, the principle of electrowetting-on-dielectric (EWOD) was implemented to overcome this prevalent issue.[63–65] With EWOD, large contact angle modulation can be achieved by replacing the EDLC with a thin dielectric layer between the liquid and the electrode, due to its ability to hold large electrostatic energy.[66,67] Furthermore, adding a hydrophobic coating to the dielectric layer can provide large initial surface energy and high reversibility.[24]

Fig. 1 presents a working principle of the EWOD mechanism for droplet actuation. A liquid droplet sits on a hydrophobic-coated dielectric layer below which an electrode plate is placed (Fig. 1a). The droplet forms its initial contact angle (θ_0) along a three-phase contact line at the equilibrium where three surface tension forces (*i.e.*, $\gamma_{SL,0}$, γ_{SG}, and γ_{LG}) are balanced. When a bias voltage is applied between the droplet and the bottom electrode, the electric energy, $c(\Delta V)^2/2$, is stored across the dielectric capacitor (c_d). This storage energy makes the electric charges re-distribute at the liquid–solid interface and decreases the surface tension force from $\gamma_{0,SL}$ to γ_{SL}. This force modification leads to the contact angle change of the droplet from θ_0 to θ (Fig. 1b). Fig. 1(c) shows an equivalent circuit consisting of two electric impedances across a liquid droplet and a dielectric layer serially connected.

To accomplish droplet actuation, an EWOD mechanism utilizes such an electrically controlled contact angle of the droplet on a solid surface. As shown in Fig. 1(d), a conventional EWOD device consists of two parallel plates sandwiching a liquid droplet in between. The top plate is a hydrophobic-coated electrode, while the bottom plate is composed of 2D arrayed pixelated electrodes covered with a hydrophobic-coated dielectric layer.[68–71] To actuate a droplet on an EWOD device, an electric potential is applied between the top electrode plate and the bottom pixelated electrode near the droplet. The droplet's contact angle correspondingly decreases to form an advancing angle (θ_{adv}) on the electrically activated electrode and a receding angle (θ_{rec}) at the other side (Fig. 1d). Consequently, a pressure gradient is created inside the droplet and drives it towards the region electrically activated. To further implement droplet transportation, the foregoing steps are repeated by sequentially activating nearby

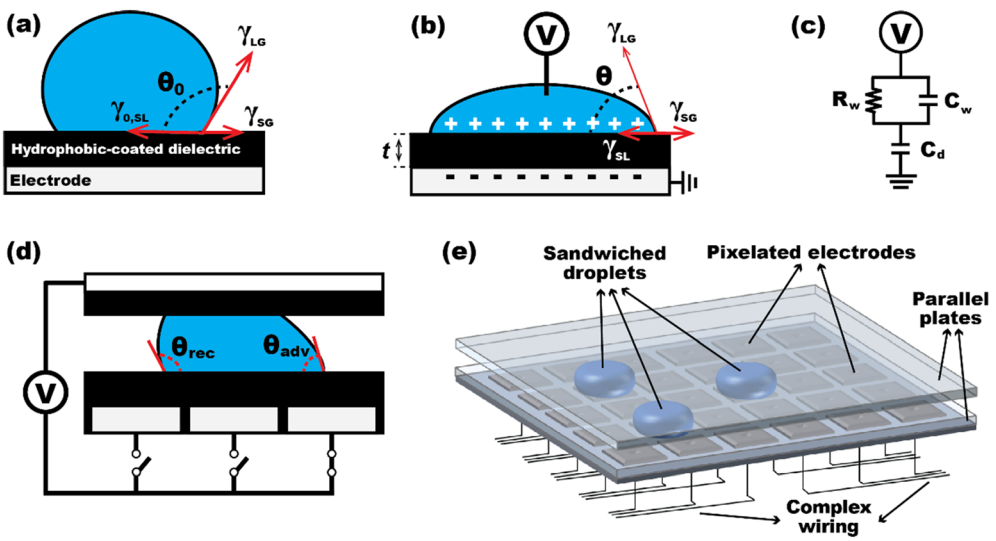

Fig. 1 A working principle of the electrowetting on dielectric (EWOD) for droplet actuation. (a) When a liquid droplet is placed on a solid surface, it forms an initial contact angle (θ_0) along a three-phase contact line at the equilibrium where three surface tension forces γ_{SL}, γ_{SG} and γ_{LG} at the solid–liquid (SL), solid–gas (SG), and liquid–gas (LG) interfaces are balanced. (b) With an electric potential applied between the liquid droplet and electrode plate, the electric charges are re-distributed and modify the surface tension at the solid–liquid interface, resulting in a decrease in the droplet contact angle. (c) An equivalent circuit model consisting of two electric impedances of the liquid droplet and dielectric layers. (d) To actuate a droplet, a bias voltage is applied between the top electrode plate and the bottom pixelated electrode near the droplet. Then, it forms an advancing contact angle (θ_{adv}) at the electrically activated electrode and a receding angle (θ_{rec}) at the other side. This creates a pressure gradient inside the droplet which drives it towards the region electrically activated. (e) Conventional EWOD devices typically encounter the issues of complex fabrication processes for patterning and wiring of 2D arrayed electrodes.

electrodes. Thus, conventional EWOD devices are appended with several drawbacks. Firstly, the minimum droplet size that can be manipulated on a device relies on the size of the physically pixelated electrode, limiting device versatility and reconfigurability. Moreover, conventional EWOD devices come with the drawback of device complexity led by complex electrode patterning and wiring issues (Fig. 1e). While the process of pixelated electrode patterning can be simplified with the use of printed circuit boards (PCBs), a tedious process of connecting each individual electrode to a wire may lead to potential interconnection problems.[72] Fabrication of an EWOD device can be susceptible to such problems when large-scale parallel manipulations of multiple droplets are required. These issues with wiring connection can be further eliminated by the via process, ultimately increasing the fabrication cost and complexity of an EWOD device.[73]

2.2 OEW-based droplet actuation

On the other hand, optoelectrowetting (OEW) technologies have been proposed as alternative solutions to address these fabrication issues arising from conventional EWOD devices. Instead of electric activation of individual electrodes on EWOD, OEW makes use of optical addressing on a photoconductive surface to induce an electrowetting effect. Fig. 2(a) shows the structure of a typical OEW device. The main distinction from EWOD is the use of a photoconductive layer between a hydrophobic-coated dielectric layer and a bottom electrode. An equivalent circuit model of the OEW shown in Fig. 2(c) can be used to understand how an electrowetting effect (*i.e.*, contact angle change of the droplet) can be induced by light illumination. It can be equivalently modelled to have three electric impedances across the layers of a liquid droplet, a dielectric, and a photoconductor, which are serially connected. To achieve droplet actuation, an alternating current (AC) voltage is applied between the liquid droplet and the bottom electrode. However, the droplet remains close to its initial contact angle on the solid surface at a dark state (*i.e.*, no light illumination), as shown in Fig. 2(a). This is because the majority of the voltage drop occurs across the photoconductive layer where electric impedance is dominant. Hence, a very small amount of voltage drop is created across the capacitance (c_d) of the dielectric layer, and the contact angle remains almost unchanged as the initial value (θ_0). To induce an OEW effect, light is illuminated onto a photoconductive layer after passing through a transparent electrode from the bottom (Fig. 2b). This generates excess electron–hole pairs at the illuminated area, leading to an increase in the photoconductivity by several orders of magnitude. As a result, the electric impedance of the photoconductivity layer significantly decreases to switch the dominance of the voltage drop (ΔV) in the dielectric layer. Correspondingly, the droplet's contact angle becomes lowered as estimated by the Young–Lippmann equation (eqn (1)).

It is worth noting that this light-enabled voltage switching effect relies on the frequency of an applied AC voltage. Using the equivalent circuit model presented in Fig. 2(c), we have studied the frequency-dependent voltage drop normalized to the input voltage. For this study, it was assumed that the thicknesses of water, dielectric, and photoconductive layers are 200 μm, 1 μm and 5 μm, respectively. An electric conductivity of a photoconductive layer was set to be $\sigma_{dark} = 1.6 \times 10^{-6}$ S m^{-1} at a dark state. Fig. 3 presents the normalized voltage drop across a dielectric layer as a function of the AC frequency for various photoconductivity ratios between illuminated and dark states (*i.e.*, $b = \sigma_{photo}/\sigma_{dark}$). At frequencies below 50 Hz, the majority of the voltage drop is created in a dielectric layer even at a dark state (*i.e.*, $b = 1$). Therefore, effective OEW modulation can't be achieved for optical droplet actuation. For frequencies above 200 Hz, there

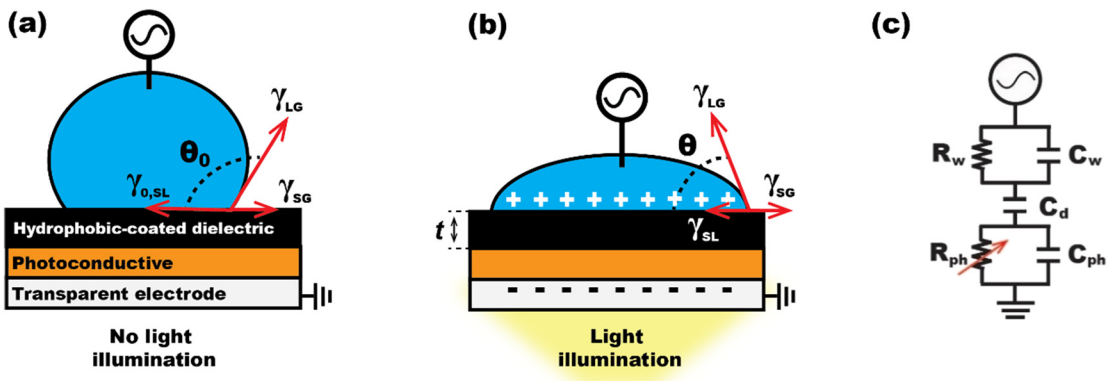

Fig. 2 A working principle of the optoelectrowetting (OEW) for optical droplet actuation. (a) An OEW device is composed of a photoconductive layer inserted between the layers of a hydrophobic-coated dielectric and an electrode. With an AC voltage applied between the liquid droplet and the bottom electrode, it forms an initial contact angle (θ_0) on the solid surface at a dark state (*i.e.*, no light illumination). (b) Upon the illumination of light from the bottom, the dominance of the electric impedance shifts from the photoconductive layer to the dielectric layer due to the increase in its conductivity. As a result, most of the voltage drop is created across the dielectric layer. This induces an electrowetting effect by decreasing the liquid droplet's contact angle to θ. (c) An equivalent circuit model of the OEW consisting of three electric impedances across the liquid droplet, dielectric, and photoconductive layers.

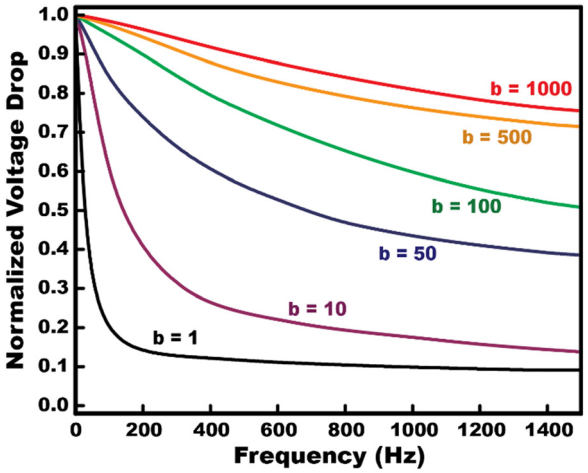

Fig. 3 Frequency-dependent voltage switching to a dielectric layer for various b values, which indicate the photoconductivity ratios (*i.e.*, $b = \sigma_{photo}/\sigma_{dark}$).

is only a small amount of voltage drop across the dielectric layer in a dark state. However, when light is illuminated onto a photoconductive layer (*i.e.*, $b > 1$), its conductivity increases to switch the dominance of the voltage drop to the dielectric layer. This voltage switching effect continues to increase with the light intensity illuminated (see Fig. 3). For example, at the AC frequency of 200 Hz, there is only 13% of the input voltage drop across the dielectric layer at a dark state, leading to a negligible contact angle change. However, upon light illumination with a photoconductivity ratio of $b = 100$, about 90% of the input voltage can be stored across the dielectric layer to contribute to OEW modulation even at the same input frequency of 200 Hz. This voltage switching effect makes significant modification in the droplet's contact angle to be used for optical droplet actuation. Another interesting observation from Fig. 3 is that the voltage switching effect begins to saturate when $b > 500$ where the electric impedance of the photoconductive layer becomes negligible.

To achieve droplet transportation, the OEW utilizes sequential addressing of a light pattern onto a continuously deposited (*i.e.*, no patterned) photoconductive surface, instead of sequential activation on pixelated electrodes near the droplet on the EWOD. This OEW mechanism can offer device simplicity by fully eliminating complex fabrication procedures (*e.g.*, photolithography) necessary for electrode patterning, wiring, and interconnection typically faced by conventional EWOD devices. Furthermore, the minimum droplet size to be manipulated on the OEW device can be flexibly controlled by simply adjusting the size of the light pattern, instead of the electrode size physically patterned on an EWOD device.

3. Conventional OEW technologies

With the benefits of device simplicity and flexibility, OEW technologies have been developed. This chapter will discuss the fundamentals of conventional OEW devices and introduce how OEW technologies have been advanced to offer device simplicity and flexibility over EWOD devices.

3.1 Early-stage OEW devices

The concept of OEW as a light-driven droplet actuation mechanism was first introduced by Chiou *et al.*[47] Fig. 4 shows schematic illustrations of the OEW device. This early-stage OEW device was similarly structured to conventional EWOD devices where a liquid droplet is squeezed between two parallel plates. The top plate of the OEW device was composed of a hydrophobic-coated electrode, while the bottom plate was much more complicated than that of EWOD devices. The bottom plate consisted of electrowetting (*i.e.*, 2D arrayed) electrodes and grid electrodes between which a photoconductive layer of amorphous silicon (a-Si) was inserted. Subsequently, silicon dioxide (SiO_2) and Teflon layers were deposited on top of the 2D arrayed electrode layer to provide dielectric and hydrophobic properties (see Fig. 4a).

To implement optical droplet actuation, an AC bias voltage was applied between the top plate and the bottom grid electrodes (Fig. 4b). As discussed in the previous section, with the absence of light illumination (*i.e.*, a dark state), the electric impedance is dominant across the a-Si layer, where

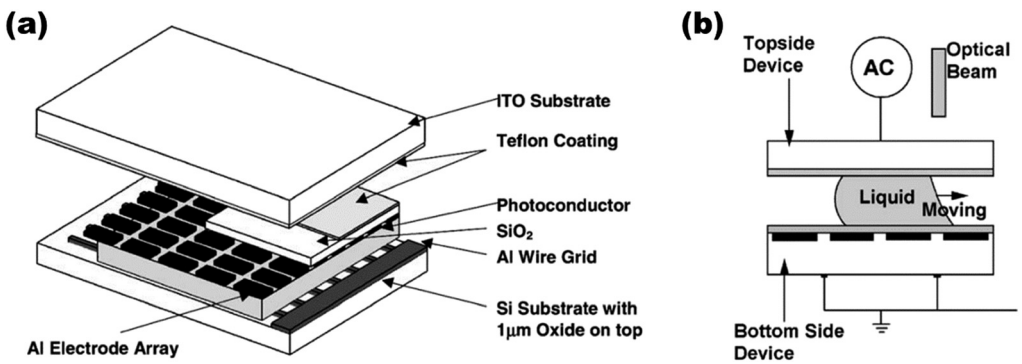

Fig. 4 An early stage optoelectrowetting (OEW) device. (a) A schematic structure of an early-stage OEW device consisting of two parallel plates. (b) Droplet actuation on the OEW device, where a liquid droplet is sandwiched between two parallel plates. Reproduced with permission from ref. 47.

the majority of the voltage drop occurs. Hence, a very small amount of voltage drop is created across the SiO_2 layer, resulting in a negligible contact angle change with no droplet actuation. However, when an optical beam illuminates one edge of the droplet, the conductivity of the a-Si layer significantly increases by several orders of magnitude and switches most of the voltage drop across the SiO_2 layer at the light illuminated area. This caused a local electrowetting effect to form the advancing angle (θ_{adv}) of the droplet. Consequently, a pressure gradient inside the droplet gives rise to the droplet actuation towards the area illuminated by the optical beam (Fig. 4b). In experiments, the transportation of a droplet (approximately 1.6 μL) has been optically accomplished on an active device area of 1.0 × 1.0 cm^2 using a 4.0 mW laser (532 nm). By applying an AC voltage of 200 V_{pp} with a frequency of 500 Hz, a droplet speed of 7.0 mm s^{-1} was demonstrated. Detailed experimental conditions and results are provided in Table 1.

Chiou *et al.* went on to further develop the OEW technology into a microfluidic system that can perform a complete set of droplet manipulation functions such as droplet injection, transportation, merging, mixing, and splitting using laser illumination controlled by programmable scanning mirrors.[74] Fig. 5 shows the device structure designed as a sandwich configuration. However, this OEW device offered easy fabrication by patterning both the 2D arrayed electrowetting electrodes and the grid electrodes on the same plane of a glass substrate, unlike the previous OEW device where the layers of the electrowetting and grid electrodes were vertically separated by the photoconductive layer. Then, these electrowetting electrodes were connected to the grid electrodes *via* photoconductive bridges made of hydrogenated amorphous silicon (a-Si:H), followed by the layers of SiO_2 and Teflon to provide dielectric and hydrophobic properties (Fig. 5a).

The droplet actuation principle of this OEW device is like that previously discussed. An AC bias voltage at 500 Hz was applied between the top and bottom grid electrodes. Under the conditions of no light illumination, the a-Si:H bridges would have an electrical impedance a few orders of magnitude greater than the SiO_2 layer. As a result, the electrowetting electrodes could not be activated, and the voltage drop across the SiO_2 layer became negligible with no contact angle modification. However, when light is illuminated near one edge of the droplet, the photoconductivity of the a-Si:H bridges would significantly increase to electrically activate the nearby electrowetting electrodes at the light illuminated area (Fig. 5b). This optical addressing on the electrodes makes the majority of the voltage drop across the top and bottom SiO_2 dielectric layers of the device induce an electrowetting effect. As the droplet contact angles at both the top and bottom plates decrease to form the θ_{adv}, an asymmetric droplet meniscus is created, where surface tension forces result in a net pressure that makes a droplet move towards the illuminated light beam. Experimentally, various droplet-based microfluidic functions, including droplet injection, transportation, splitting, and multi-droplet manipulations, have been successfully demonstrated on the OEW device with an active area of 1.0 × 1.0 cm^2, using a 5.0 mW laser (532 nm) as the light source. A maximum droplet actuation speed of 78 mm s^{-1} was achieved with a 0.4 μL water droplet.

Drawbacks. By utilizing the optical method to activate the electrowetting electrodes, these early-stage OEW devices eliminated complex wiring issues typically faced by conventional EWOD devices, such as the need to individually connect large numbers of 2D arrayed electrodes. However, since these OEW devices were similarly designed to EWOD, device fabrication was still complicated due to the photolithographic processes required for patterning of 2D arrayed electrodes and photoconductive bridges.

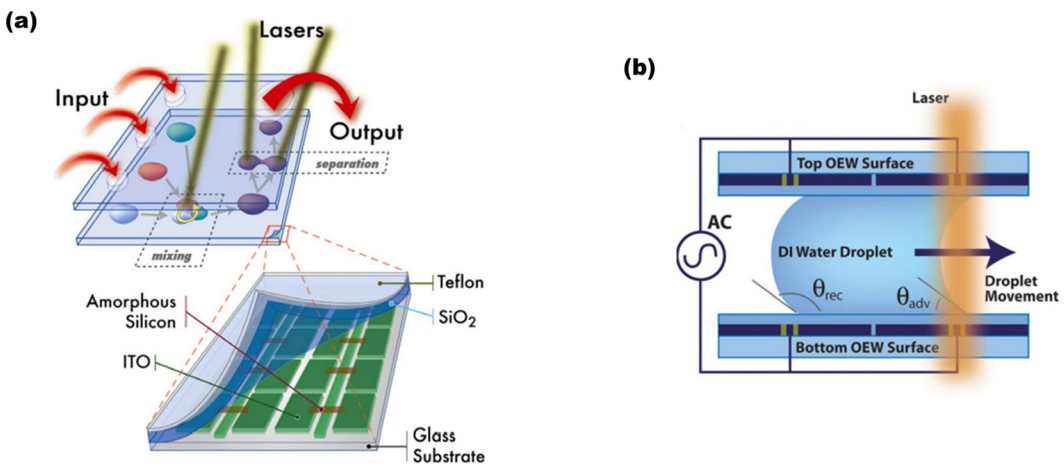

Fig. 5 An OEW-based microfluidic system. (a) The complete set of droplet manipulation functions such as droplet injection, transportation, merging, mixing, and splitting has been demonstrated using the OEW technology as an active-type microfluidic system. (b) Droplet actuation on the OEW. Reproduced with permission from ref. 74.

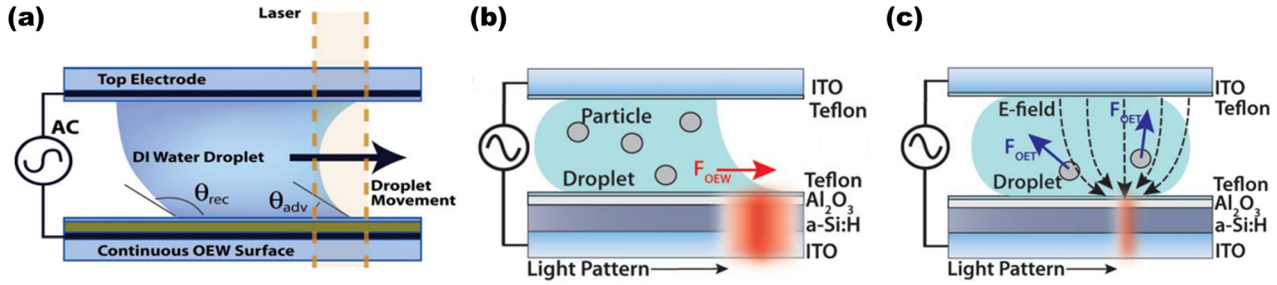

Fig. 6 Continuous optoelectrowetting (COEW). (a) A COEW device configuration can be fabricated with several featureless layers by eliminating patterning processes. When a light pattern is illuminated on a continuous photoconductive film, it creates a localized electric field concentration resulting in a net electro-mechanical force on the liquid droplet. (b) A united COEW device enables both OEW-based droplet transportation at f = 10 kHz and (c) dielectrophoretic (DEP) manipulation of single cells within a droplet at f = 200 kHz by simply adjusting the AC frequency applied at the same platform. Reproduced with permission from ref. 58 and 76.

3.2 Continuous optoelectrowetting (COEW)

To address the fabrication issue of the early-stage OEW devices, a continuous (*i.e.*, no patterned) optoelectrowetting (COEW) mechanism has been proposed.[75–77] It was designed as a sandwich configuration similar to the previous OEW,[47,74] but with the photoconductive and electrode layers continuously deposited. As shown in Fig. 6(a), the top plate consisted of a transparent ITO electrode covered with a hydrophobic-coated dielectric layer. The bottom plate, however, provided an OEW surface made up of several featureless layers in the order of hydrophobic-coated dielectric and photoconductive layers on top of an electrode layer. Not only did these continuous layers fully eliminate the need for patterning processes (*e.g.*, photolithography) to facilitate device fabrication, but they also enabled a droplet to be flexibly positioned at any location on the featureless photoconductive surface to allow continuous droplet transportation. The working principle of the COEW device is similar to that of the previous OEW devices. While applying an AC bias voltage between the top and bottom electrodes, most of the input voltage drop is created within the a-Si layer due to its dominant electrical impedance under the conditions of no light illumination. This meant that the voltage drop across the SiO_2 layer is very small, resulting in no droplet movement. To achieve droplet actuation, a light beam is illuminated near a droplet. Thus, the photoconductivity of the a-Si layer locally increases by several orders of magnitude, forming a virtual electrode due to the generation of excess electron–hole pairs at the illuminated area. This significantly reduces its electrical impedance and shifts most of the voltage drop to the SiO_2 layer. Consequently, the droplet's contact angle decreases to form an advancing angle (θ_{adv}), driving it towards the light illuminated area. Using a 0.8 mW HeNe laser (632 nm) as a light source, transportation of droplets in a picoliter volume (10–50 pL) has been achieved on a continuous photoconductive surface at a speed of 1.0 mm s^{-1}.

Later, Pei *et al.* improved the COEW performance by replacing SiO_2 with aluminum oxide (Al_2O_3) as the dielectric layer deposited by an atomic layer deposition (ALD) method.[78] With the Al_2O_3 layer offering a higher dielectric constant than the SiO_2 layer, the magnitude of the AC bias voltage applied on a COEW device could be reduced to as low as 16 V_{pp}. In addition, instead of a laser beam used in previous studies,[47,74] an optical projector with as much as 85-fold lower light intensity was used to induce virtual electrodes on the OEW surface of the device. Experimentally, large-scale manipulation of liquid droplets ranging from 5 nL to 2 μL has been demonstrated at a droplet actuation speed of 2.0 cm s^{-1} on the COEW device surface. Furthermore, Valley *et al.* have presented a unified COEW platform that enabled both OEW and dielectrophoretic (DEP) operations for on-chip manipulation of droplets as well as particles by simply altering the applied AC frequency.[58] The device performed both OEW-based droplet manipulation in volumes ranging from 12.5 to 335 nL at 10 kHz (Fig. 6b) and dielectrophoretic (DEP) manipulation of individual cells (diameter ~10 μm) inside a droplet at 200 kHz (Fig. 6c) using an optical projector (<1.0 W cm^{-2}). Valley *et al.* have demonstrated OEW droplet actuation at a speed of up to 8.0 mm s^{-1}.

Drawbacks. Compared to early-stage OEW devices designed with 2D arrayed electrowetting electrodes and photoconductive bridges, the COEW mechanism has offered easy device fabrication with a featureless (*i.e.*, no patterned) surface where a droplet can be positioned at any location of the device. Furthermore, the minimum droplet size governed by the size of the physically patterned electrodes typically observed in early-stage OEW devices has been fully eliminated on the continuous surface. Nevertheless, the COEW device still faces the issue of device interfacing with other microfluidic components due to its sandwich (*i.e.*, closed) structure. This closed device configuration seriously limited its flexibility and extensibility with integration of external microfluidic components (*e.g.*, external reservoirs, optical detectors).

3.3 Open optoelectrowetting (o-OEW)

An open optoelectrowetting (o-OEW) configuration has been later proposed to eliminate this deficiency.[53,79] Unlike the

previously discussed OEW studies, the o-OEW device has an open (*i.e.*, single-sided) configuration, but still consists of patterned electrodes covered with a hydrophobic-coated dielectric layer on a photoconductive (a-Si) layer. Its working principle is similar to that previously discussed. With an AC bias voltage applied to the patterned electrodes, light illumination enabled local modification of the electrical impedance in the photoconductive layer, and further dominance of the voltage drop (ΔV) across the dielectric layer at the illuminated area. This light-enabled switching effect on the voltage drop makes the droplet's contact angle decrease for optical droplet actuation. Using a 3.0 mW laser (670 nm) as a light source, droplet transportation at a speed of as fast as 3.6 mm s^{-1} was achieved. More recently, Loo *et al.* developed another variation of o-OEW by integrating a conductive metal grid mesh onto the OEW surface of the device.[51] The device demonstrated OEW-based dispensing and merging of 1 μL droplets using a 1.5 W cm^{-2} optical projector, achieving a droplet speed of 4.5 cm s^{-1}.

Drawbacks. Nevertheless, the o-OEW still shares the limitations of early-stage OEW devices. Not only are the patterning processes of 2D arrayed electrodes still required, but also the minimum droplet size that can be manipulated on an o-OEW device has remained constrained by the size of the arrayed electrodes.

4. Further developments in OEW

The increasing attractiveness of optoelectrowetting (OEW) has seen the technology progress over the past few years. In this section, further developments and advances in OEW technologies will be discussed.

4.1 Single-sided continuous optoelectrowetting (SCOEW)

To overcome the main issues highlighted by all previous OEW studies,[47,53,58,74–79] Park *et al.* have developed a new OEW mechanism, called single-sided continuous optoelectrowetting (SCOEW).[80] This SCOEW mechanism combines the benefits from both the COEW and o-OEW devices. It has a single-sided (*i.e.*, open) configuration that ensures a flexible interface for easy integration with other external microfluidic components (*e.g.*, optical detectors, reagent reservoirs, microchannel devices, *etc.*) and easy accessibility to reagent droplets placed on an open surface. At the same time, a continuous and featureless configuration offers the device simplicity in fabrication as well as high versatility and extensibility by eliminating the limitation of the minimum droplet size and allowing droplets to be continuously positioned at any location on a 2D planar surface. More importantly, unlike all previous OEW devices, the operation of the SCOEW mechanism is based on a lateral field modulation. This SCOEW mechanism allows the use of low-intensity light sources such as an LCD display (as much as 4 orders of magnitude lower intensity than lasers or optical projectors commonly used in previous OEW studies) without any additional optical components such as lenses. These unique aspects of the SCOEW will be detailed in the following sections.

Fig. 7 shows schematic illustrations of the SCOEW device in a single-sided continuous configuration. The device fabrication begins with the deposition of a photoconductive (a-Si:H) layer on a glass substrate using plasma enhanced chemical vapor deposition (PECVD). On top of the a-Si:H layer, only two aluminum (Al) electrodes are required to be patterned at both edges of the device. Then, an amorphous fluorocarbon polymer, called Cytop, was spin-coated to provide hydrophobic and dielectric properties. Compared to the previous OEW devices, the continuous configuration of the SCOEW offers simple device fabrication without any photolithographic processes for patterning and wiring of 2D arrayed electrowetting electrodes.

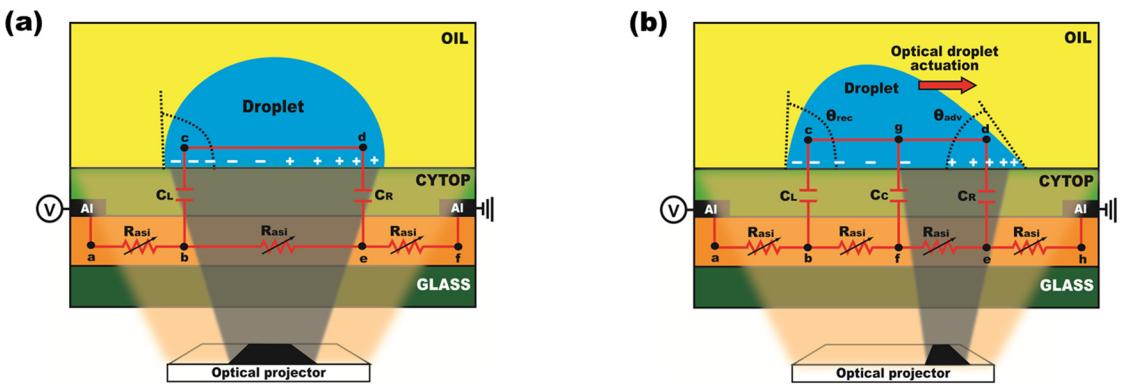

Fig. 7 Single-sided continuous optoelectrowetting (SCOEW). A schematic of the SCOEW device is shown with its equivalent circuit model. (a) When a dark pattern is symmetrically illuminated in the middle of the droplet, the photo-resistance increases at the area illuminated by the dark pattern. However, ΔV across the capacitors at both edges of the droplet increases by the same magnitude such that $\Delta V_{bc} = \Delta V_{de}$ which corresponds to the droplet spreading out symmetrically to have a contact angle of θ. (b) When a dark pattern is illuminated onto one side of the droplet, the photo-resistance asymmetrically increases, causing a voltage drop difference at the droplet edges (*i.e.* $\Delta V_{bc} > \Delta V_{de}$). As the contact angle decreases to form an advancing angle, θ_{adv}, the asymmetric droplet shape creates a pressure gradient inside the droplet that actuates it in the direction of the dark pattern. Reproduced with permission from ref. 80.

The droplet actuation principle on the SCOEW can be qualitatively explained using an equivalent circuit model presented in Fig. 7. Unlike the previous OEW mechanisms, the SCOEW utilizes a direct current (DC) bias voltage applied between the two electrodes positioned at the edges of the device. Thus, a uniform electric field is generated along the lateral direction to form a shunt circuit, where the photoconductive layer can be equivalently modeled as photoresistors in a series connection and the dielectric layer is equivalent to capacitors in a parallel connection. Since the electric conductivity of the liquid droplet is much higher as compared to the other layers, its electrical impedance can be neglected. Under the uniform electric field distributed along a lateral direction, the droplet remains almost symmetrical with its initial contact angle θ_0 in an oil medium, resulting in no droplet actuation. When a dark pattern is illuminated in the middle of the droplet (Fig. 7a), the photo-resistance of the a-Si:H layer increases only at the area (between nodes b and e) illuminated by the dark pattern, and the voltage drop (*i.e.*, ΔV_{be}) correspondingly increases as well. However, this voltage drop can be equally divided across two capacitors c_L and c_R at the edges of the droplet (*i.e.*, $\Delta V_{bc} = \Delta V_{de} = 1/2\Delta V_{be}$). These equal voltage drops maintain the droplet symmetrically with the same contact angles on both sides, leading to no droplet movement. However, in the case of asymmetric illumination, where a dark pattern is projected onto one side of the droplet (Fig. 7b), the photo-resistance of the a-Si:H layer increases at the dark illuminated area, resulting in an asymmetrical increase in the voltage drop at the corresponding side of the droplet (*i.e.*, $\Delta V_{bc} \neq \Delta V_{de}$). This leads to the formation of the advancing (θ_{adv}) and receding (θ_{rec}) contact angles to actuate the droplet towards the direction of the dark pattern illuminated.

When compared to prior OEW studies,[47,53,58,74–79] the SCOEW mechanism provides an important and unique feature for droplet actuation. Due to the formation of a shunt equivalent circuit composed of dielectric capacitors and photoresistors (see Fig. 7), the electrowetting voltages across the two capacitors c_L and c_R are determined by the relative ratio of photo-resistances between nodes b and e, not by their absolute values. Therefore, even a 2-fold ratio in the photoconductivity between the illuminated and non-illuminated sites, *i.e.*, $b = 2$, is sufficient to induce droplet actuation. This unique characteristic allows optical actuation of droplets with a low optical intensity for large area manipulations on a SCOEW device. With this interesting characteristic, later SCOEW studies have demonstrated the use of a smartphone as a low-intensity light source and the use of a polymer-based low-quality photoconductive material to offer cost-effective, portable, lab-on-a-chip (LOC) platforms.[50,55,56]

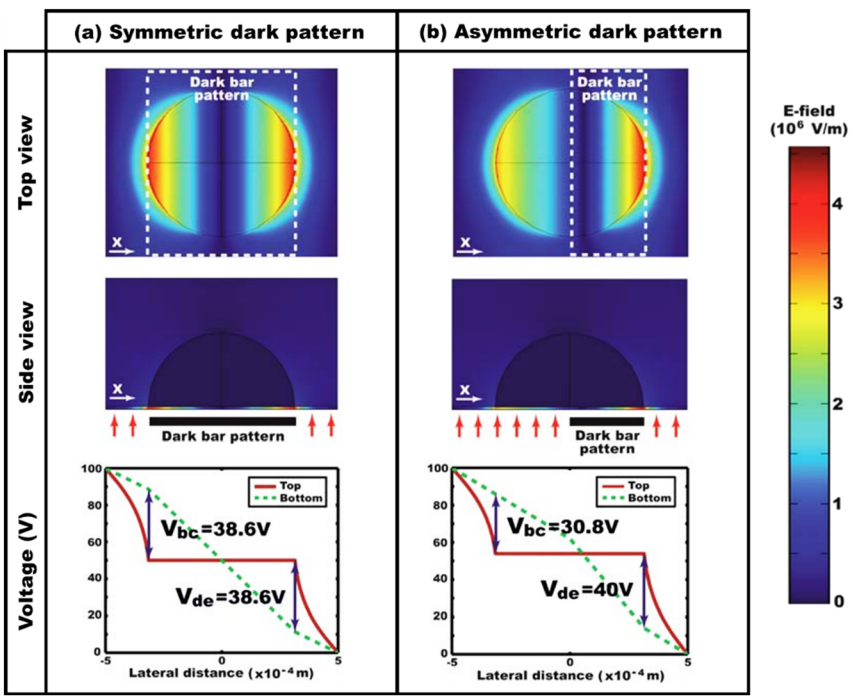

Fig. 8 3D numerical simulation results showing electric field distribution and voltage profiles under various dark pattern illumination. (a) When a dark pattern as wide as the base diameter of the droplet is symmetrically projected in the middle of the droplet, the voltage drops are equal on both droplet edges ($\Delta V_{bc} = \Delta V_{de} = 38.6$ V) as the droplet spreads out symmetrically to have a contact angle of 90° with no droplet actuation. (b) When a dark pattern half the size of the droplet is asymmetrically illuminated on one side of the droplet, the resistance of the a-Si–H layer asymmetrically increases at the only area illuminated by the dark pattern. As a result, the voltage drops at the droplet edges are differently created (*i.e.*, $\Delta V_{bc} = 30.8$ V $< \Delta V_{de} = 40.0$ V), causing the advancing (θ_{adv}) and receding (θ_{rec}) angles to optically drive the droplet towards the dark pattern projected. Reproduced with permission from ref. 80.

Numerical simulation studies. The droplet actuation principle mentioned above for the SCOEW has been validated by 3D simulation studies implemented using COMSOL Multiphysics.[80] For the simulation studies, a hemispherical water droplet was modelled to be positioned on the device composed of 10 μm dielectric, 5 μm photoconductive, and 550 μm thick electrically insulating-dielectric oil layers. A DC bias voltage of 100 V was applied at both end planes separated by a 1.0 mm gap to provide a uniform electric field along a lateral direction. To represent a low-quality photoconductive property, the electric conductivity of the photoconductive layer was assumed to be $\sigma_{photo} = 2 \times 10^{-8}$ S m^{-1} at a photo state and $\sigma_{dark} = 1 \times 10^{-8}$ S m^{-1} at a dark state with an only 2-fold ratio (*i.e.*, $b = 2$). Fig. 8 presents the simulation results of the electric field distribution as the top and side views, and the voltage profiles under: (a) symmetric illumination of a dark pattern and (b) asymmetric illumination of a dark pattern. The voltage distribution profiles extracted from the top (solid lines) and bottom (dotted lines) surfaces of the dielectric layer are depicted. The voltage differences between these top and bottom surfaces of the dielectric layer indicate the voltage drops, ΔV_{bc} and ΔV_{de}, at the left and the right edge of the droplet, which determine the advancing (θ_{adv}) and receding (θ_{rec}) angles of the droplet as estimated by the Young–Lippmann equation (eqn (1)). In Fig. 8(a), when a dark-bar shaped pattern is symmetrically projected in the middle of the droplet, a 2-fold photo-resistance increases only at the area illuminated by the dark pattern. However, no droplet actuation can be achieved due to the equal voltage drops (*i.e.*, $\Delta V_{bc} = \Delta V_{de} = 38.6$ V) at both edges of the droplet. On the other hand, in Fig. 8(b), a dark pattern asymmetrically projected to one side of the droplet causes an increase in the photo-resistance only at the area illuminated by the dark pattern. As a result, the droplet undergoes an unbalanced voltage drop (*i.e.*, $\Delta V_{bc} = 30.8$ V $<$ $\Delta V_{de} = 40.0$ V) at its edges, causing the advancing (θ_{adv}) and receding (θ_{rec}) angles to optically drive the droplet towards the dark pattern projected. This simulation study has verified the droplet actuation principle of the SCOEW that is based on relative voltage control, as discussed in Fig. 7.

Experimental demonstrations. Fig. 9(a) and (b) depict continuous light-actuated droplet transportation on a SCOEW device using a commercially available optical projector as a light source to provide dynamic light patterns. Interestingly, by simply adjusting the size of a dark pattern, droplet transportation could be achieved in a wide range of the droplet volumes from 50 μL (Fig. 9a) to 250 pL (Fig. 9b) on the same SCOEW device without any extra optical components (*i.e.*, lenses for light focusing). To further demonstrate the requirement of a low-intensity light source, Fig. 9(c) shows the device being gently placed on an LCD computer monitor that provides 4 orders of magnitude lower light intensity than lasers or optical projectors commonly used for previous OEW studies. With a 1.3 mm wide dark pattern directly illuminated from an LCD monitor without any extra lens, a 0.5 μL water droplet could be optically transported at a speed of 510 mm s^{-1}. Various other droplet manipulation functions were demonstrated as well. Fig. 9(d) presents the splitting of a 1 μL droplet by the sudden illumination of a 6 mm wide dark pattern. In Fig. 9(e), two water droplets, one 0.5 μL (dissolved with a green dye) and one 2 μL, experienced electrocoalescence for merging due to the dipole–dipole interaction between the two droplets. To mix the contents in the combined droplet, the droplet was optically driven across the SCOEW device surface by a moving dark pattern. This process created a shear force from the bottom, which caused an internal flow to induce droplet mixing.

The capability of SCOEW for integration with other microfluidic components on a single-sided surface has also been demonstrated. For example, the schematic illustration in Fig. 10(a) depicts an external sample reservoir being integrated with a SCOEW device through a pin connector. With dynamic optical patterns being programmed onto the

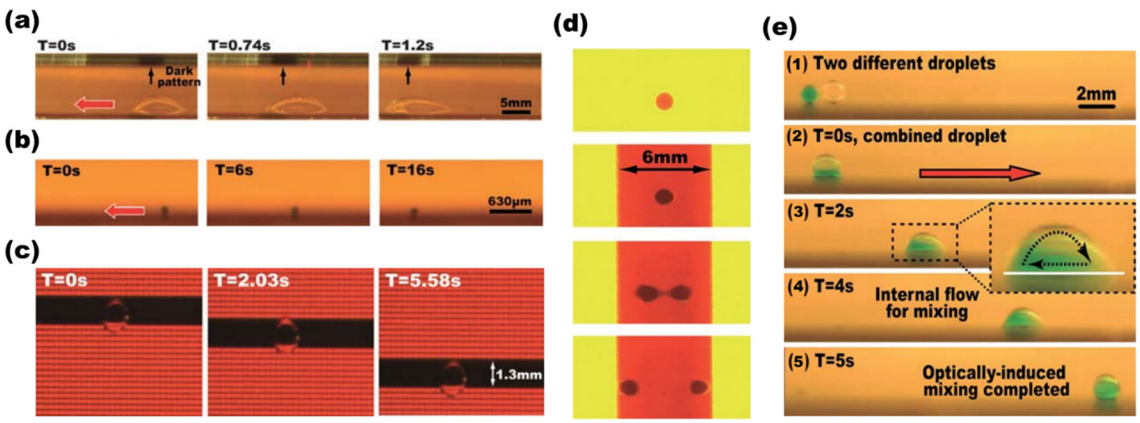

Fig. 9 Various light-driven droplet manipulations with the SCOEW. Experimental demonstrations of continuous transportations of water droplets with volumes of (a) 50 μL and (b) 250 pL by simply adjusting the size of a dark pattern. (c) To realize the requirement of a low-intensity light source, actuation of a 0.5 μL droplet on an LCD display was conducted. Other droplet manipulation functions such as (d) splitting of a 1 μL droplet and (e) merging and mixing of two droplets (0.5 μL and 2 μL) were also demonstrated. Reproduced with permission from ref. 80.

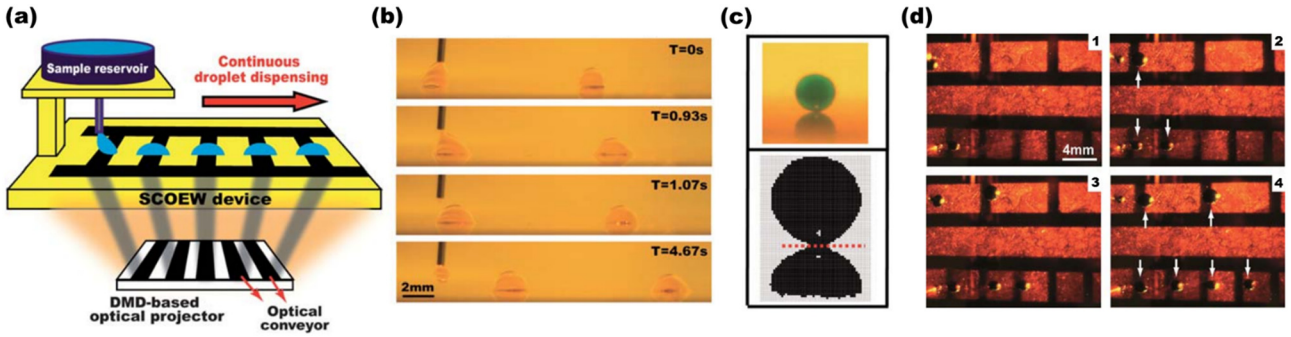

Fig. 10 The capability of SCOEW for flexible integration with other microfluidic components. (a) A schematic drawing of an external sample reservoir being integrated into the SCOEW for light-triggered droplet injection. (b) 2.5 μL droplets being continuously injected from the sample reservoir into a SCOEW chamber. (c) Image analysis of the injected droplets with less than 1% in volume variation, demonstrating precise volume control of the SCOEW. (d) Experimental demonstrations of parallel light-triggered droplet injection from two external reservoirs, where 1.8 μL (top conveyor) and 0.9 μL droplets (bottom conveyor) were continuously injected and transported along the SCOEW surface with different periodicities. Each snapshot (1)–(4) was taken with a 12.94 s time delay. Reproduced with permission from ref. 80.

SCOEW device, droplet injection can be triggered from the sample reservoir. Fig. 10(b) shows video snapshots of the light-triggered droplet injection, where 2.5 μL water droplets were continuously injected from the sample reservoir into a SCOEW chamber at a constant speed of 1 mm s^{-1}. To highlight precise droplet volume dispensing on the SCOEW, digital images of the injected droplets were analyzed with an image processing toolbox (using MATLAB). As indicated in Fig. 10(c), it was examined that there was less than 1% in volume variation between the injected droplets. Further demonstrations on parallel light-triggered droplet injection are presented in Fig. 10(d). Using two dark bar conveyors moving at the same speed but with different periodicities, 1.8 μL (top conveyor) and 0.9 μL droplets (bottom conveyor) were continuously injected from two separate reservoirs and successfully transported along the SCOEW surface.

Later, Shekar *et al.* developed another SCOEW device using a 25 nm thin Al_2O_3 layer as a dielectric.[52] This dielectric layer helped to increase the effective capacitance of the dielectric region, thereby reducing the required threshold voltage for droplet manipulation by as much as 2 orders of magnitude. The device was patterned with multiple electrodes for multi-directional droplet manipulations. By using a 1.5 W cm^{-2} optical projector with a lateral electric field of 24 V cm^{-1}, a maximum transportation speed of 12 mm s^{-1} can be achieved with a 20 μL droplet. More recently, Liu *et al.* demonstrated multidimensional droplet manipulation along arbitrary directions on a SCOEW device by projecting Z-shaped optical patterns.[81] In experiments with an applied electric field of 80 V cm^{-1} (in the *x*-direction), an 8 μL droplet can be transported in the *y*-direction (perpendicular to the direction of the electric field) at a maximum speed of 4.86 mm s^{-1}.

4.2 Flexible SCOEW device for 3D droplet manipulation

With technological advances in EWOD over the past few years, research attention has been further extended to three-dimensional (3D) spatial control of droplets on a non-planar EWOD surface. Not only can this 3D EWOD technology allow larger volumetric capacities, but it can also provide much more flexibility and functionality than two-dimensional (2D) planar devices. Relevant studies of 3D EWOD technology have been widely demonstrated, including droplet actuation on uneven terrains,[82–84] vertical translation,[85–88] droplet jumping,[89–92] even in the form of wearable wristbands for portable point-of-care (POC) applications,[93,94] and new fabrication methods of 3D devices.[95–97] Despite such numerous studies on 3D EWOD technology, it was challenging for OEW researchers to demonstrate light-driven 3D droplet manipulations on flexible substrates due to the incompatibility of depositing photoconductive materials that have been commonly used for previous OEW devices onto flexible substrates. Park's group has recently presented a flexible SCOEW technology to overcome this critical issue by utilizing a polymer-based photoconductive material.[50]

As discussed earlier, all previous OEW studies have used the a-Si material to provide photoconductive properties.[47,53,58,74–80] However, an issue associated with the a-Si material is the requirement of conventional integrated circuit (IC) processes such as chemical vapor deposition (CVD) or plasma enhanced chemical vapor deposition (PECVD) for its thin-film layer deposition.[98–100] These IC fabrication processes typically require complex and expensive laboratory setups like high vacuum facilities and have to be operated at high temperatures of over 300 °C.[100,101] Nevertheless, most of the commercially available flexible substrates such as polyethylene terephthalate (PET) and polyethylene naphthalate (PEN) detrimentally experience thermal deformation under such high-temperature conditions of over 300 °C.[102,103] This compatibility issue has seriously prevented OEW devices from being fabricated on flexible substrates for 3D droplet applications. Jiang *et al.* overcame such a compatibility issue by substituting the a-Si material with titanium oxide phthalocyanine (TiOPc), which is a polymer-based

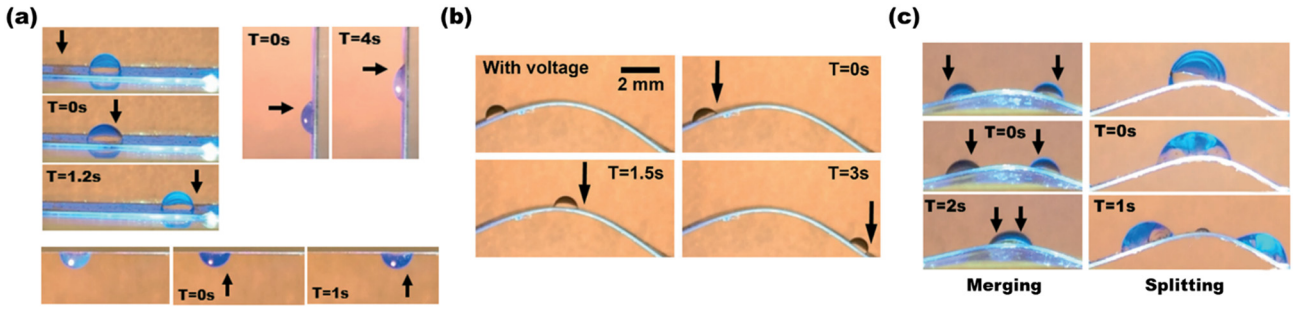

Fig. 11 Light-driven 3D droplet manipulations with flexible SCOEW technology. (a) Experimental demonstrations of droplet transportations on various 3D terrains such as flat, vertical, and upside-down surfaces. (b) 3D droplet transportation is also achieved on a curved surface. (c) Droplet-based functions of merging and splitting on a curved surface are also demonstrated. Black arrows indicate locations of the projected dark patterns. Reproduced with permission from ref. 50.

photoconductive material.[50] The use of TiOPc as a photoconductive material has enabled simple device fabrication on a flexible substrate *via* a low-cost, spin-coating method, thereby fully eliminating the need for complex and expensive high-temperature processes such as CVD or PECVD. The concept of the flexible SCOEW technology has been experimentally demonstrated, as presented in Fig. 11. In Fig. 11(a), liquid droplets were optically manipulated on various types of 3D terrains, including a flat surface (an inclined angle, φ = 0°), a vertical surface (φ = 90°), and an upside-down surface (φ = 180°). 3D droplet transportation on a curved surface is experimentally demonstrated in Fig. 11(b). In addition, the capabilities of SCOEW for droplet merging and splitting have been further demonstrated on a 3D curved surface (Fig. 11c).

Previous OEW studies have typically focused on experimental demonstrations of droplet actuation in various device configurations, while Jiang *et al.* have interestingly discussed about analytical studies to estimate the light-induced EWOD force.[50] This analytical prediction helped us to understand an optimum size of the dark pattern relative to the droplet size at a given value of b (*i.e.*, a photoconductivity ratio) to maximize the OEW force. With small values of b less than 10, which represent low-quality photoconductive materials or low-intensity light illumination, the OEW force can be maximized by a dark pattern with half the size of the droplet size. As the value of b increases, the force sharply increases even at a small pattern size. This is because the small dark pattern is sufficient in creating a large voltage drop to maximize the OEW force due to the large conductivity change between photo and dark states, when the b value is high. For example, when $b = 10^3$, representing high-quality photoconductive materials or high-intensity light illumination, the OEW force is estimated to be as high as 45 μN (>11-fold larger compared to that when b = 5) by projecting a dark pattern as wide as a tenth of the droplet size.

Drawbacks. With the use of TiOPc as a photoconductive material, the flexible SCOEW technology can offer several benefits over previous OEW devices, such as low-cost and simple device fabrication and device flexibility and functionality through 3D spatial droplet manipulations on non-planar terrains. However, it has one critical drawback with regard to its low-quality photoconductive property. As reported in previous OEW studies,[47,50] the photoconductive performance of the TiOPc material is not as significant as that of the a-Si material. In other words, the b value of the a-Si is in the magnitude of a few orders, whereas that of the TiOPc is in the range of a few folds. This poor photoconductive property of the TiOPc material is caused by its limited charge carrier mobility and low exciton diffusion length at the donor/acceptor interface.[104,105] To facilitate charge transport, a thin layer of TiOPc is required. However, a thin TiOPc layer will result in insufficient light absorption.[106] This greatly reduces the effect of optical activation on the OEW device, which results in a much smaller OEW force induced as compared to high-quality photoconductors like the a-Si material. Hence, OEW devices would not be able to operate effectively as droplet manipulation tools. This limitation in light absorption associated with the TiOPc material has been later overcome by utilizing plasmonic nanoparticles, which will be detailed in the next section.

4.3 Plasmonic-enhanced SCOEW

Thio *et al.* have developed a plasmonic-enhanced SCOEW technology to offer significant improvements in light absorption of TiOPc by using metal nanoparticles.[107] For this study, the device was fabricated to have metal nanoparticles randomly dispersed on top of the TiOPc layer *via* a spin-coating method before deposition of a hydrophobic-coated dielectric layer, as shown in Fig. 12. With the presence of nanoparticles, light rays that have been transmitted (*i.e.*, did not get absorbed) through the TiOPc active layer will undergo plasmonic light scattering, which effectively increases their optical path length over a wide angular spread within the TiOPc layer. Thus, more light rays can be redirected back onto the TiOPc layer resulting in significantly enhanced light absorption to improve the photo-state conductivity of the TiOPc material. On the other hand, the dark-state

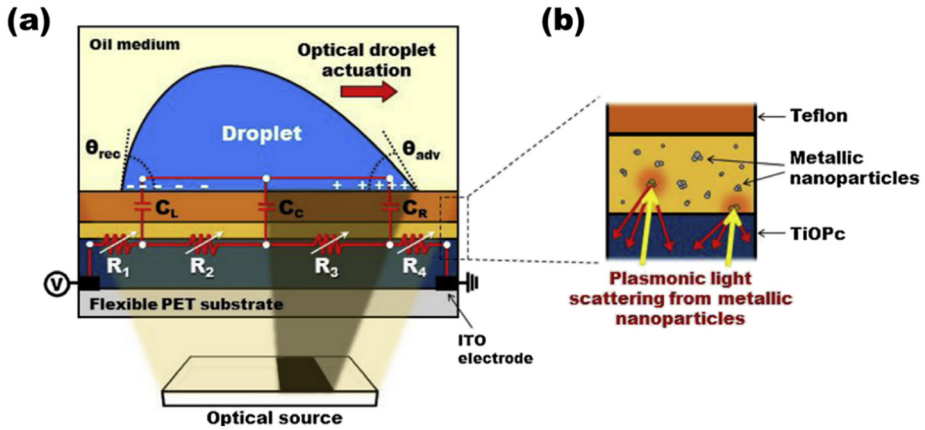

Fig. 12 Plasmonic-enhanced SCOEW technology. (a) Plasmonic nanoparticles are used to improve light absorption in the photoconductive layer of a SCOEW device. (b) With the presence of a nanoparticle layer, light rays that are not absorbed by the TiOPc active layer will undergo plasmonic light scattering. As a result, their optical path lengths increase over a wide angular spread as more light rays are redirected back onto the TiOPc layer, enhancing light absorption and OEW performance. Reproduced with permission from ref. 107.

conductivity of the TiOPc material at the dark illuminated area remains unchanged. This enhanced conductivity switching performance ($b = \sigma_{photo}/\sigma_{dark}$) of the TiOPc material can increase the OEW performance with much larger forces.

Several numerical simulation studies have supported the phenomenon of plasmonic light scattering and redirection back onto the TiOPc layer by adding a layer of conductive nanoparticles. Fig. 13(a) presents how the optical path lengths of incoming light rays have been increased after being scattered by a single metallic nanoparticle (50 nm in diameter) over a wide angular spread. The scattered light intensity of each ray matches well with the Rayleigh theory, which attributes light absorption of a nanoparticle to its angular dependence on plasmonic light scattering.[108,109] From another simulation study, Fig. 13(b) and (c) depict a total of 20 000 input light rays being illuminated onto an array of uniformly distributed conductive nanoparticles in 3 staggered layers. Results have shown that only 22.05% of the

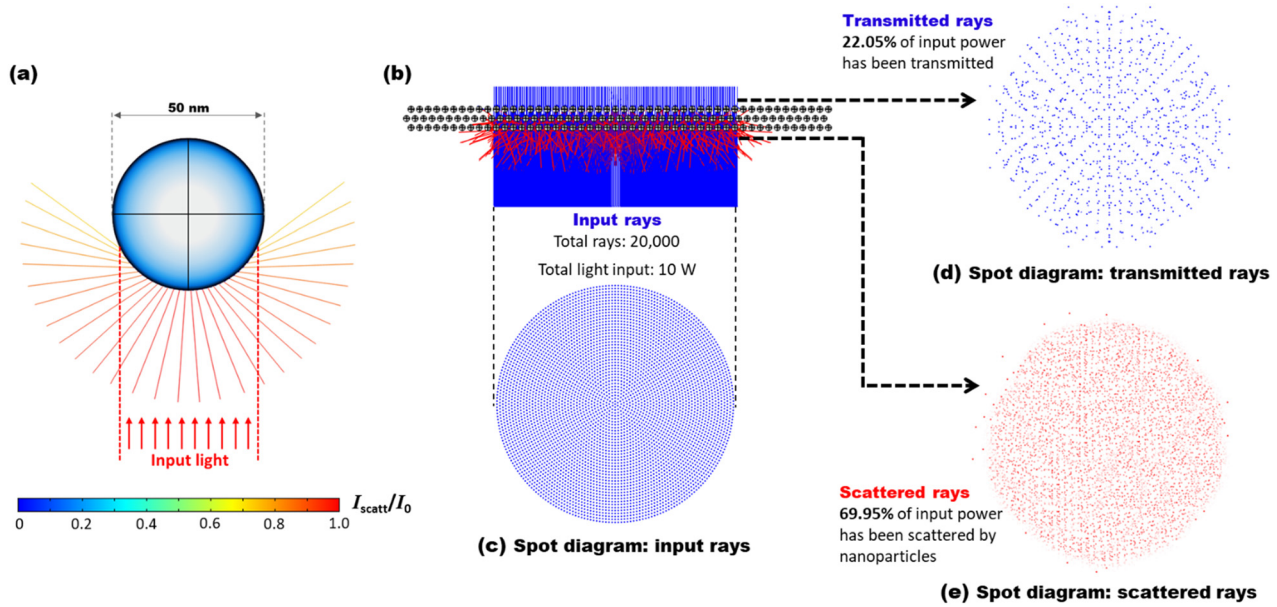

Fig. 13 Simulation results of plasmonic light scattering. (a) Input rays increase their optical path lengths after being scattered by a single nanoparticle over a wide angular spread. The angular dependence of a scattered ray intensity means that a lower scattered intensity (I_{scatt}) as compared to the input ray (I_0) is obtained at a larger direction of scattering. (b) and (c) A total of 20 000 input light rays are projected onto an array (3 staggered layers) of uniformly distributed conductive nanoparticles. (d) Only 22.05% of the input power emerged from the top as transmitted rays, while (e) 69.95% of the input power emerged from the bottom as scattered rays. The use of nanoparticles above the low-quality TiOPc photoconductive layer in an OEW device encourages plasmonic light scattering to redirect more light rays onto the TiOPc layer, greatly improving its light absorption and photo-state conductivity. Reproduced with permission from ref. 110.

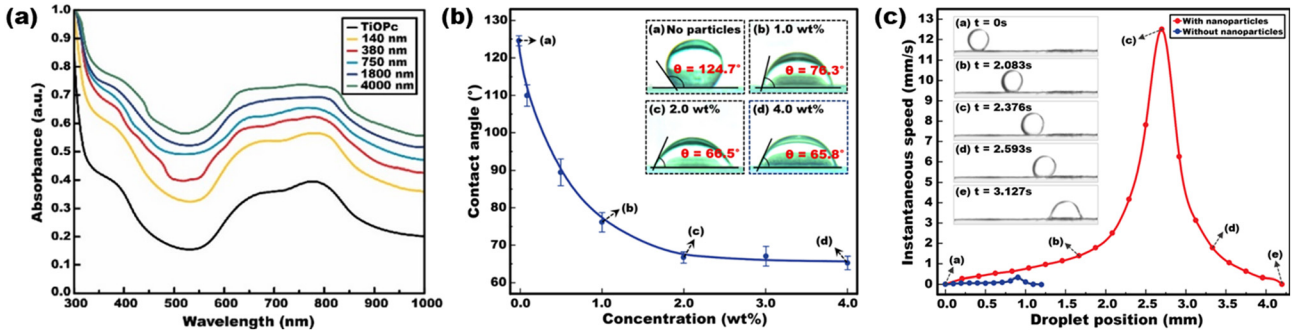

Fig. 14 Experimental demonstrations for plasmonic-enhanced SCOEW. (a) Spectrometric absorbance of a TiOPc layer coated with 2.0 wt% Al nanoparticles at various thicknesses. Light absorption has been greatly enhanced because of plasmonic light scattering from the nanoparticles. (b) Measurements of a droplet's static contact angle indicating that a larger contact angle modulation can be attained with higher nanoparticle concentrations. (c) Light-driven droplet dynamics demonstrating a droplet speed as high as 12.5 mm s^{-1} due to the presence of nanoparticles, which is 39 times faster than the case without the use of nanoparticles. Reproduced with permission from ref. 107.

input power emerged from the top of the nanoparticle array as transmitted rays (Fig. 13d), while 69.95% of the input power was detected from the bottom as scattered rays. The remaining 8% of the input power was accounted for by the power lost due to the angular-dependent light absorption properties of the nanoparticles (as described in Fig. 13a) as well as the continued propagation of rays within the nanoparticle arrays. These simulation studies demonstrated how input rays are angularly scattered by the nanoparticles before being redirected back onto the TiOPc layer to additionally contribute to the layer's light absorption and photo-state conductivity.

The plasmonic-enhanced OEW performance was also experimentally demonstrated. In Fig. 14(a), a spectrophotometric absorbance study indicated the dramatic enhancement in light absorption of the TiOPc layer with the use of thicker layers of Al nanoparticles (at 2 wt% concentration). Another study on a droplet's static contact angle verified that an increasingly larger contact angle modulation can be attained with higher nanoparticle concentrations, showing as much as 58.9° (*i.e.*, $\Delta\theta$ = 124.7° − 65.8°) more contact angle modulation than the case without nanoparticles (Fig. 14b). These two experimental studies demonstrated that the thicker or denser the layer of the nanoparticles, the higher the optical absorption onto the TiOPc layer and the higher the contribution to the electrowetting effect. Lastly, a light-driven droplet dynamics study in Fig. 14(c) recorded a droplet instantaneous speed as high as 12.5 mm s^{-1} with the presence of nanoparticles, which is 39 times faster than the case without any use of nanoparticles.

The plasmonic-enhanced OEW technology utilizes conductive nanoparticles to induce plasmonic light scattering onto the TiOPc layer, thereby increasing its light absorption and photo-state conductivity. This technology provides a significantly improved OEW performance for effective light-driven droplet manipulation even with a poor-quality TiOPc layer, thus offering cost effectiveness of devices in numerous potential droplet microfluidic applications.

5. OEW applications as portable smartphone-integrated environmental sensors

Water is the most essential resource for all living forms on Earth. There are various species in water systems even including viruses and bacteria. Timely detection of any hazards (*e.g.*, toxic dinoflagellates, *Vibrio* spp., *etc.*) existing in water systems and rapid communication of relevant information with a central host are very important to properly manage water quality without contamination and pollution of water systems.[111,112] However, conventional methods are inefficient, costly, and labor-intensive, requiring large volumes of water samples and time-consuming laboratory-level examinations for water quality detection.[113–115] To address these issues, several smartphone-integrated SCOEW studies have been proposed. In this section, the emergence of OEW technology as smartphone-integrated portable biosensors will be introduced for environmental applications.

5.1 A smartphone-based fluorescence microscope for real-time and on-site detection of harmful algae cells

With the SCOEW's benefits of device simplicity, cost effectiveness, versatility, and flexibility, Jiang *et al.* developed a smartphone-integrated optoelectrowetting (SiOEW) device to offer a portable method that is low-cost and simple for on-site water quality detection.[56] Fig. 15 shows a schematic of the SiOEW platform to work as a portable fluorescence microscope for on-site detection of target cells in environmental water. A commercially available smartphone, which was placed below the SCOEW device, was utilized as a low-intensity portable light source (a few orders of magnitude lower intensity than lasers and optical projectors used for previous OEW studies) to illuminate dynamic optical patterns onto the photoconductive surface of the device. Using the OEW principle, various droplet-based microfluidic functions (*e.g.*, transportation, mixing, and immobilization on a

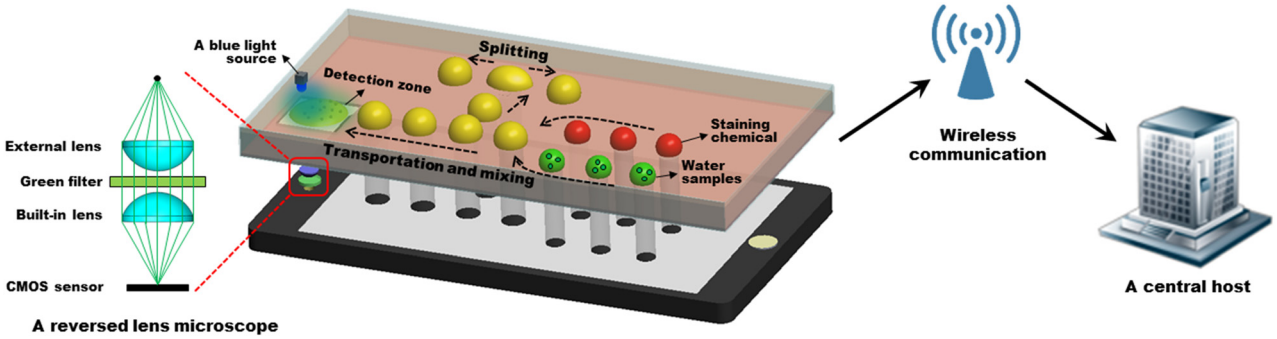

Fig. 15 The smartphone integrated optoelectrowetting platform (SiOEW). The SiOEW platform is able to perform on-chip water sample preparation and on-site monitoring of water quality. The smartphone is used to project low-intensity light patterns onto a SCOEW device for OEW-based droplet manipulation. At the same time, the smartphone allows on-chip fluorescence microscopy for the detection of target algae cells in water samples by mounting several optical components above its built-in camera to form a reversed lens microscope. Finally, the smartphone can rapidly share its location and the captured data with a central host (*e.g.*, an environmental agency). Reproduced with permission from ref. 56.

hydrophobic-coated detection zone) were carried out for on-chip processing of water samples.

To equip the SiOEW with the capability for on-chip fluorescence microscopy detection of the target algae cells in water samples, a reversed smartphone lens microscope was developed using two identical smartphone lens modules and a green bandpass filter inserted between the lens modules.[116] This reversed lens microscope has ensured a full coverage of the smartphone's complementary metal-oxide-semiconductor (CMOS) sensor due to the perfectly matched angular field of views of the identical lens modules. With the presence of a blue LED light bulb for fluorescence excitation, only the stained target cells in water samples are detected using the smartphone's built-in digital camera after passing through the reversed lens microscope that allows up to 45× magnification for on-chip water quality analyses. Additionally, the smartphone is equipped with various functions such as wireless communications and global positioning system (GPS) capability. These capabilities allow captured data (*e.g.*, location tracking, time of test conducted) to be shared instantly and wirelessly with a central host (*e.g.*, an environmental regulation agency) for real-time monitoring and management of water quality.

To further improve device portability for on-site water quality detection, Lee *et al.* developed a 3D-printed hand-held SiOEW platform, where various optical and electrical components such as a smartphone, an external lens module, a voltage source and a SCOEW device were compactly assembled together (see Fig. 16a).[117,118] This hand-held SiOEW platform is capable of performing on-chip water sample preparation as well as rapid and *in situ* monitoring of viable algae in water samples directly collected from local reservoirs and coastline. For experimental demonstrations of on-chip fluorescence microscopy detection, Fig. 16(b) and (c) present the digital images of harmful algae cells in a freshwater sample spiked with *C. reinhardtii* and a marine water sample spiked with *Amphiprora* sp. that were captured using the smartphone's digital camera. A smartphone app was further used to count the populations of the harmful algae cells in the water samples. In Fig. 16(d), a cell counting

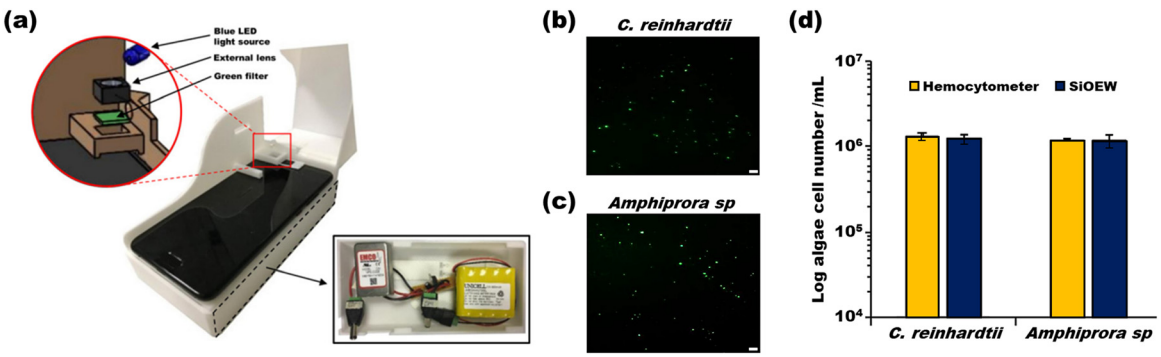

Fig. 16 An automated 3D-printed SiOEW platform. (a) A 3D-printed platform housing all the optical and electrical components together to enhance device portability. These components include a smartphone, SCOEW device, lens module, and voltage source. On-chip fluorescence microscopy detection and digital images of harmful algae cells in (b) a freshwater sample spiked with *C. reinhardtii* and (c) a marine water sample spiked with *Amphiprora* sp. captured using an integrated smartphone. (d) Cell counting comparison between a regular microscopy method using a hemocytometer and the SiOEW approach, showing cell populations in the same orders of magnitude. Reproduced with permission from ref. 117.

comparison between a regular microscopy method (*i.e.*, using a hemocytometer) and the SiOEW approach is presented. The measured cell population data show that the 3D-printed SiOEW platform can provide comparable results for the target cell counting in the same orders of magnitude as the hemocytometer.

5.2 A lab-on-a-smartphone (LOS) platform for on-site detection of fecal contamination in water *via* the LAMP assay

Being able to provide rapid and on-site detection of waterborne pathogens in environmental water essentially safeguards public health from the dangers of fecal contamination. In recent years, Thio *et al.* developed another smartphone-integrated SCOEW platform, called a lab-on-a-smartphone (LOS), as a portable, low-cost, and fully integrated system that enables rapid, *in situ* monitoring of fecal indicator bacteria (FIB) and their associated pathogens in environmental water without the need for sophisticated laboratory equipment or skilled personnel.[55] The LOS was developed as a portable platform where three main components, a plasmonic-enhanced OEW device, a transparent heater, and a commercially available smartphone, are compactly integrated to eliminate the need for auxiliary optical and mechanical components (*e.g.*, pumps and tubes to feed individual reagents, microscope and CCD camera for microscopy analyses) typically required for a conventional lab-on-a-chip (LOC) setup. As shown in Fig. 17(a) and (b), a plasmonic-enhanced OEW device performs pumpless and tubeless droplet manipulations for on-chip water sample preparations of fecal indicator bacteria (FIB) and the corresponding LAMP mixture in an oil chamber. Secondly, the integration of a transparent heater to the bottom surface of the plasmonic-enhanced OEW device equips the LOS platform with the capability to conveniently perform LAMP assays for *in situ* analysis of water quality. This enabled on-chip isothermal nucleic acid amplification at 65 °C without bulky and expensive equipment like a thermal cycler (Fig. 17c). Lastly, various features on the integrated smartphone can eliminate the need for auxiliary equipment and components. For example, a smartphone's display screen serves as a low-intensity light source to project dynamic light patterns onto the photoconductive surface of the plasmonic-enhanced OEW device for effective optical manipulation of oil-immersed water samples. Due to the single-sided, open-chamber configuration of the LOS, the smartphone can also be easily integrated as a portable optical detector to conveniently implement on-chip molecular detection of FIB (Fig. 17d). For a real-time colorimetric assessment of the LAMP assay results, the smartphone's built-in camera was first used to capture digital images of the target water samples. Next, its image processing app was further used for quantitative analysis of time-dependent color changes of the target samples by computing their red–green–blue (RGB) values.

Fig. 18(a) shows an experimental demonstration of on-chip *E. coli* sample processing on a plasmonic-enhanced OEW device, where two droplets of 1.0 μL freshwater spiked

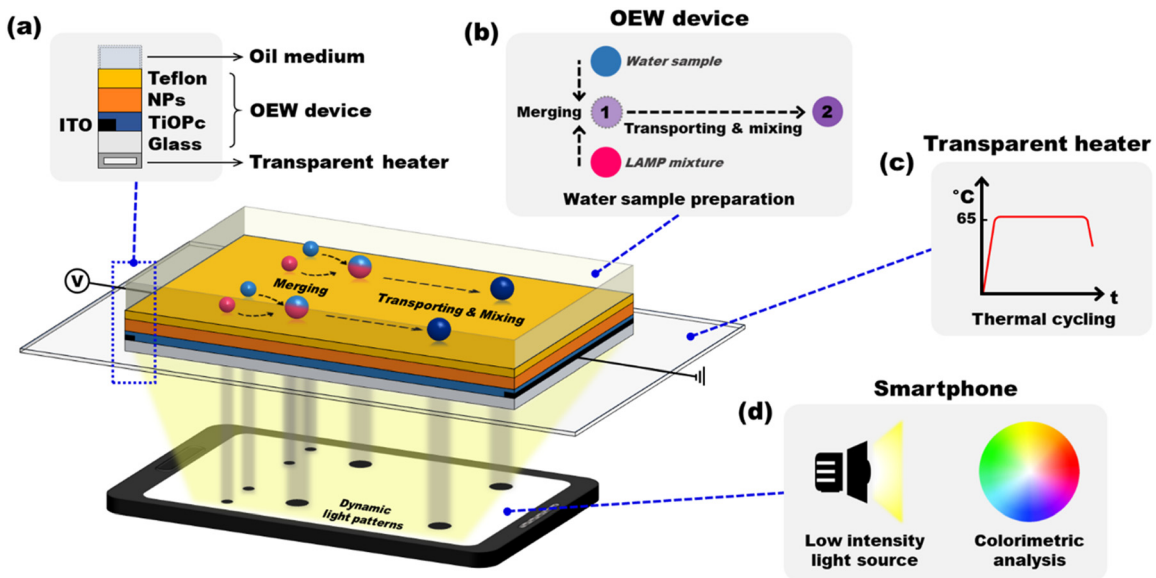

Fig. 17 A lab-on-a-smartphone (LOS) platform for on-site detection of water quality through portable LAMP testing. (a) and (b) The LOS platform that integrates plasmonic-enhanced OEW technology with a transparent heater and a smartphone. The OEW device allows on-chip LAMP mixture and water sample preparations with light-driven OEW droplet manipulations, with low-intensity light patterns illuminated by the smartphone below. (c) A transparent heater provides the heating conditions to perform isothermal nucleic acid amplifications for LAMP assays. (d) A smartphone has a secondary function of serving as a portable colorimetric analyzer during the LAMP reaction. The LOS platform can perform rapid assessment of environmental water samples *via* LAMP assays without requiring any bulky and sophisticated laboratory equipment or skilled personnel. Reproduced with permission from ref. 55.

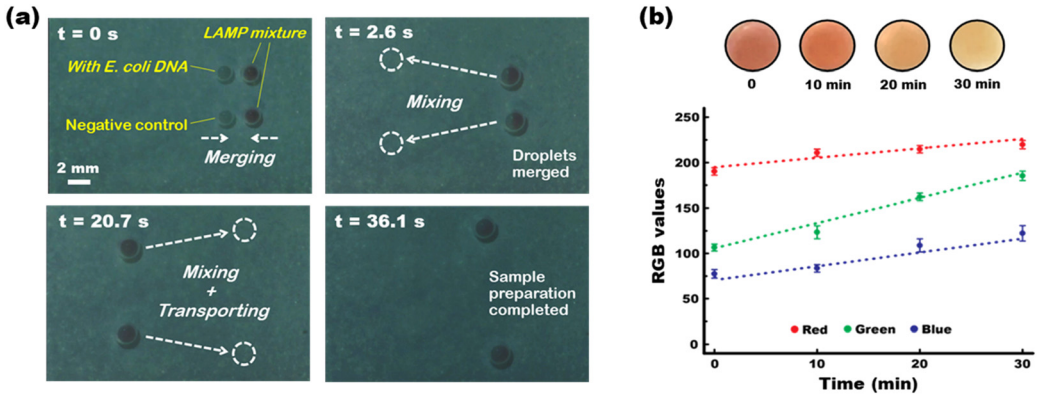

Fig. 18 Experimental demonstrations on the LOS. (a) On-chip *E. coli* sample processing with a 1.0 μL freshwater droplet spiked with *E. coli* DNA and a 1.5 μL droplet of the LAMP mixture. (b) LAMP assay results and smartphone-based colorimetric detection. Reproduced with permission from ref. 55.

with *E. coli* DNA and a 1.5 μL LAMP mixture were successfully merged, transported, and mixed when dynamic optical patterns were projected from a smartphone placed below. Fig. 18(b) presents the digital images of the droplet taken at 10 min intervals throughout the entire duration of the LAMP reaction using the smartphone's digital camera. The positive LAMP assay showed that the color of the reaction mixture gradually changed from pink to yellow, indicating a successful DNA amplification. Using the smartphone's app, this colorimetric observation was further quantified *via* the time-dependent RGB-based analysis. A distinct difference in the RGB values was quantitatively indicated to validate the successful amplification of the target DNA sequence.

A SCOEW device can perform on-chip sample preparation effectively with multiplexed droplet manipulation functions. The integration of a smartphone with the OEW technology promises a simple yet powerful, portable LOS platform that can be greatly beneficial for numerous environmental applications. This LOS platform is potentially useful for *in situ* microbiological monitoring of environmental water due to its ability to deliver rapid and reliable test results in resource-limited settings without requiring any bulky and complex laboratory equipment or skilled personnel.

6. Conclusion and outlook

OEW technologies have been emerging as solutions for effective light-driven droplet manipulations with the benefits of device functionality, reconfigurability, adaptability, and cost effectiveness and showing great promise for various lab-on-a-chip applications. This review paper presents the fundamentals, research progress and innovations of OEW technologies. Conventional OEW-based devices can be categorized into: (1) early-stage OEW, (2) COEW, and (3) o-OEW. These OEW-based devices have a similar droplet actuation principle, where the optical addressing on a photoconductive surface modifies its electrical impedance and shifts the majority of the voltage drop to the dielectric layer to induce a localized electrowetting effect. In early-stage OEW devices, a liquid droplet is sandwiched between two parallel plates, with the bottom plate consisting of an OEW surface and an array of 2D patterned electrodes. However, they have several drawbacks, including complexity in device fabrication and difficulty in interfacing with other microfluidic components. In COEW, the patterned electrodes have been replaced with a continuous (featureless) photoconductive layer, where virtual electrodes can be created on the photoconductive layer upon light illumination. This allows continuous transportation of liquid droplets and eliminates the issue with droplet size limitation. However, COEW devices still face similar fabrication complexity and interfacing difficulty due to their sandwich configuration. Such a deficiency was eliminated in o-OEW by adopting an open (single-sided) configuration. Nevertheless, like the conventional OEW, the physically patterned electrodes give rise to the issues of device extensibility and flexibility by limiting the minimum droplet size to be manipulated.

Further innovations to OEW-based devices have been investigated. Notably, the development of the SCOEW eliminates the limitations due to its single-sided open configuration structure, continuous photoconductive layer, and no pixelated electrodes. The lateral field modulation in the SCOEW allowed the use of low-intensity light sources such as an LCD display for optical droplet manipulations without any additional optical components. Next, the introduction of the flexible SCOEW technology, which utilized the polymer-based TiOPc as a spin-coatable photoconductive material, offers several benefits over the previous OEW devices, such as low-cost simple device fabrication and device flexibility and functionality by allowing light-driven 3D droplet manipulations on a flexible substrate. Additionally, the use of plasmonic nanoparticles further enabled improvement of the OEW performance by enhancing the light absorption and photo-state conductivity of the TiOPc layer. The plasmonic-enhanced SCOEW technology has demonstrated improvement in the droplet actuation speed by as much as 39 fold.

With the benefit of effective optical droplet manipulation, recent progress has seen OEW devices being incorporated with commercially available smartphones. Not only was a smartphone's display used as a portable, programmable, and low-intensity light source for automated OEW droplet manipulations, but also the vast capabilities of a smartphone and its wide range of mobile apps allow it to work as an optical detector or a convenient tool for instant wireless communication of the detected information. Such capabilities enable smartphone-integrated OEW devices to be reliable and portable environmental sensors. This paper further reviews a plasmonic-enhanced OEW device integrated with a smartphone, which has been developed as a portable biosensor that is capable of performing accurate fluorescence microscopy detection of harmful algae cells as well as LAMP assays for rapid and *in situ* monitoring of fecal contamination in environmental water.

Although the OEW technology has shown great promise for potential LOC applications, it still has room for even further developments if given considerable time and effort. More research efforts can be made to further improve several aspects of the OEW technology, including low-cost fabrication techniques, reliable device operation, and effective droplet manipulation with low voltage and low power optics requirements. Likewise, the OEW technology can be further optimized to allow parallel manipulations of even larger arrays of liquid droplets, thereby massively boosting its functionality in environmental sensing applications. Moreover, by continuously tapping into the vast capabilities of a smartphone, the smartphone integrated OEW technology has the potential to develop into low-cost, portable biosensors for a broad range of future environmental and biomedical applications.

Author contributions

Conceptualization: S. K. Thio, S.-Y. Park; funding acquisition: S.-Y. Park; supervision: S.-Y. Park; visualization: S. K. Thio, S.-Y. Park; writing – original draft: S. K. Thio; writing – review & editing: S.-Y. Park.

Conflicts of interest

There are no conflicts to declare.

Acknowledgements

This work was partially supported by the NSF CAREER Award (ECCS – 2046134), USA.

References

1 E. Brouzes, M. Medkova, N. Savenelli, D. Marran, M. Twardowski, J. B. Hutchison, J. M. Rothberg, D. R. Link, N. Perrimon and M. L. Samuels, *Proc. Natl. Acad. Sci. U. S. A.*, 2009, **106**, 14195–14200.
2 S.-Y. Park, S. Kalim, C. Callahan, M. A. Teitell and E. P. Y. Chiou, *Lab Chip*, 2009, **9**, 3228–3235.
3 A. Huebner, S. Sharma, M. Srisa-Art, F. Hollfelder, J. B. Edel and A. J. deMello, *Lab Chip*, 2008, **8**, 1244–1254.
4 S.-Y. Park and P.-Y. Chiou, *Advances in OptoElectronics*, 2011.
5 J. Wang, J. Wang, L. Feng and T. Lin, *RSC Adv.*, 2015, **5**, 104138–104144.
6 J. A. Olzmann and P. Carvalho, *Nat. Rev. Mol. Cell Biol.*, 2019, **20**, 137–155.
7 S.-Y. Park, T.-H. Wu, Y. Chen, M. A. Teitell and P.-Y. Chiou, *Lab Chip*, 2011, **11**, 1010–1012.
8 N. Wen, Z. Zhao, B. Fan, D. Chen, D. Men, J. Wang and J. Chen, *Molecules*, 2016, **21**, 881.
9 D. M. Headen, J. R. García and A. J. García, *Microsyst. Nanoeng.*, 2018, **4**, 1–9.
10 M. Navi, N. Abbasi, M. Jeyhani, V. Gnyawali and S. S. Tsai, *Lab Chip*, 2018, **18**, 3361–3370.
11 S.-Y. Park, T.-H. Wu, Y. Chen, S. Nisperos, J. F. Zhong and P.-Y. Chiou, presented in part at the Proceeding of the 14th International Conference on Miniaturized Systems for Chemistry and Life Sciences (μTAS 2010), Groningen, Netherlands, October, 2010.
12 M. Azizi, M. Zaferani, S. H. Cheong and A. Abbaspourrad, *ACS Sens.*, 2019, **4**, 841–848.
13 K. Hsieh, K. E. Mach, P. Zhang, J. C. Liao and T.-H. Wang, *Acc. Chem. Res.*, 2021, 260–266.
14 A. M. Kaushik, K. Hsieh and T. H. Wang, *Wiley Interdiscip. Rev.: Nanomed. Nanobiotechnol.*, 2018, **10**, e1522.
15 S. C. Kim, I. C. Clark, P. Shahi and A. R. Abate, *Anal. Chem.*, 2018, **90**, 1273–1279.
16 M. Pellegrino, A. Sciambi, S. Treusch, R. Durruthy-Durruthy, K. Gokhale, J. Jacob, T. X. Chen, J. A. Geis, W. Oldham and J. Matthews, *Genome Res.*, 2018, **28**, 1345–1352.
17 D.-K. Kang, M. M. Ali, K. Zhang, E. J. Pone and W. Zhao, *TrAC, Trends Anal. Chem.*, 2014, **58**, 145–153.
18 Y.-C. Tan, K. Hettiarachchi, M. Siu, Y.-R. Pan and A. P. Lee, *J. Am. Chem. Soc.*, 2006, **128**, 5656–5658.
19 C. Frey, K. Göpfrich, S. Pashapour, I. Platzman and J. P. Spatz, *ACS Omega*, 2020, **5**, 7529–7536.
20 L. Shang, Y. Cheng and Y. Zhao, *Chem. Rev.*, 2017, **117**, 7964–8040.
21 O. D. Velev, B. G. Prevo and K. H. Bhatt, *Nature*, 2003, **426**, 515–516.
22 S.-Y. Park, C. Pan, T.-H. Wu, C. Kloss, S. Kalim, C. E. Callahan, M. Teitell and E. P. Y. Chiou, *Appl. Phys. Lett.*, 2008, **92**, 151101.
23 D. Chugh and K. V. Kaler, *Microfluid. Nanofluid.*, 2010, **8**, 445–456.
24 A. R. Wheeler, *Science*, 2008, **322**, 539–540.
25 J. Cao, Q. An, Z. Liu, M. Jin, Z. Yan, W. Lin, L. Chen, P. Li, X. Wang and G. Zhou, *Sens. Actuators, B*, 2019, **291**, 470–477.
26 K. Mogi, S. Adachi, N. Takada, T. Inoue and T. Natsume, *Appl. Sci.*, 2019, **9**, 2406.
27 T. Lee and S.-Y. Park, *Micromachines*, 2021, **12**, 320.

28 Z. Jiao, X. Huang, N.-T. Nguyen and P. Abgrall, *Microfluid. Nanofluid.*, 2008, **5**, 205–214.
29 M. L. Cordero, D. R. Burnham, C. N. Baroud and D. McGloin, *Appl. Phys. Lett.*, 2008, **93**, 034107.
30 B. J. Won, W. Lee and S. Song, *Sci. Rep.*, 2017, **7**, 1–9.
31 K. Zhang, Q. Liang, S. Ma, X. Mu, P. Hu, Y. Wang and G. Luo, *Lab Chip*, 2009, **9**, 2992–2999.
32 M. A. Bijarchi, A. Favakeh, E. Sedighi and M. B. Shafii, *Sens. Actuators, A*, 2020, **301**, 111753.
33 G. Huang, M. Li, Q. Yang, Y. Li, H. Liu, H. Yang and F. Xu, *ACS Appl. Mater. Interfaces*, 2017, **9**, 1155–1166.
34 H. Moon, A. R. Wheeler, R. L. Garrell and J. A. Loo, *Lab Chip*, 2006, **6**, 1213–1219.
35 A. R. Wheeler, H. Moon, C. A. Bird, R. R. Ogorzalek Loo, C.-J. C. Kim, J. A. Loo and R. L. Garrell, *Anal. Chem.*, 2005, **77**, 534–540.
36 V. Srinivasan, V. K. Pamula and R. B. Fair, *Anal. Chim. Acta*, 2004, **507**, 145–150.
37 C. E. Clement and S.-Y. Park, *Appl. Phys. Lett.*, 2016, **108**, 191601.
38 C. E. Clement, S. K. Thio and S.-Y. Park, *Sens. Actuators, B*, 2017, **240**, 909–915.
39 R. A. Hayes and B. J. Feenstra, *Nature*, 2003, **425**, 383–385.
40 S.-Y. Park and Y. Nam, *Micromachines*, 2017, **8**, 3.
41 P. Y. Paik, V. K. Pamula and K. Chakrabarty, *IEEE Transactions on Very Large Scale Integration (VLSI) Systems*, 2008, vol. 16, pp. 432–443.
42 J. Cheng, S. Park and C.-L. Chen, *Sol. Energy*, 2013, **89**, 152–161.
43 V. Narasimhan, D. Jiang and S.-Y. Park, *Appl. Energy*, 2016, **162**, 450–459.
44 S. K. Thio, D. Jiang and S.-Y. Park, *Lab Chip*, 2018, **18**, 1725–1735.
45 T. Krupenkin and J. A. Taylor, *Nat. Commun.*, 2011, **2**, 448.
46 Q. Chen, S. J. Oh and M. Burhan, *Appl. Energy*, 2020, **269**, 115128.
47 P. Y. Chiou, H. Moon, H. Toshiyoshi, C. J. Kim and M. C. Wu, *Sens. Actuators, A*, 2003, 22–228.
48 C. Palma and R. D. Deegan, *Langmuir*, 2018, **34**, 3177–3185.
49 S. Arscott, *Sci. Rep.*, 2011, **1**, 184.
50 D. Jiang and S.-Y. Park, *Lab Chip*, 2016, **16**, 1831–1839.
51 J. Loo, S. N. Pei and M. C. Wu, *J. Opt. Microsyst.*, 2021, **1**, 034001.
52 V. Shekar, M. Campbell and S. Akella, presented in part at the 2013 IEEE International Conference on Robotics and Automation, Karlsruhe, Germany, October, 2013.
53 A. Kumar, H.-S. Chuang and S. T. Wereley, *Langmuir*, 2010, **26**, 7656–7660.
54 T. Thomas and H. N. Unni, *Microfluid. Nanofluid.*, 2019, **23**, 1–12.
55 S. K. Thio, S. W. Bae and S.-Y. Park, *Sens. Actuators, B*, 2022, **358**, 131543.
56 D. Jiang, S. Lee, S. W. Bae and S.-Y. Park, *Lab Chip*, 2018, **18**, 532–539.
57 H.-S. Chuang, H.-Y. Ku, F.-T. Li, A. Kumar, J.-C. Wang and K.-C. Wang, in *Essentials of Single-Cell Analysis*, Springer, 2016, pp. 159–194.
58 J. K. Valley, S. NingPei, A. Jamshidi, H.-Y. Hsu and M. C. Wu, *Lab Chip*, 2011, **11**, 1292–1297.
59 M. G. Lippmann, *Ann. Chim. Phys.*, 1875, **5**, 494–549.
60 F. Mugele and J.-C. Baret, *J. Phys.: Condens. Matter*, 2005, **17**, 705–774.
61 V. Narasimhan and S.-Y. Park, *Langmuir*, 2015, **31**, 8512–8518.
62 J. Varghese, H. Wang and L. Pilon, *J. Electrochem. Soc.*, 2011, **158**, A1106.
63 H. Moon, S. K. Cho, R. L. Garrell and C.-J. Kim, *J. Appl. Phys.*, 2002, **92**, 4080–4087.
64 M. G. Pollack, R. B. Fair and A. D. Shenderov, *Appl. Phys. Lett.*, 2000, **77**, 1725–1726.
65 J. Lee, H. Moon, J. Fowler, T. Schoellhammer and C.-J. Kim, *Sens. Actuators, A*, 2002, **95**, 259–268.
66 W. C. Nelson and C.-J. C. Kim, *J. Adhes. Sci. Technol.*, 2012, **26**, 1747–1771.
67 F. Saeki, J. Baum, H. Moon, J.-Y. Yoon, C. Kim and R. Garrell, *Polym. Mater.: Sci. Eng.*, 2001, **85**, 12–13.
68 D. Brassard, L. Malic, F. Normandin, M. Tabrizian and T. Veres, *Lab Chip*, 2008, **8**, 1342–1349.
69 J. Gong, *Lab Chip*, 2008, **8**, 898–906.
70 Y.-H. Chang, G.-B. Lee, F.-C. Huang, Y.-Y. Chen and J.-L. Lin, *Biomed. Microdevices*, 2006, **8**, 215–225.
71 G. J. Shah, A. T. Ohta, E. P.-Y. Chiou and M. C. Wu, *Lab Chip*, 2009, **9**, 1732–1739.
72 S. H. Byun, J. Yuan, M. G. Yoon and S. K. Cho, *J. Micromech. Microeng.*, 2015, **25**, 035019.
73 Z. Yi, H. Feng, X. Zhou and L. Shui, *Front. Phys.*, 2020, **8**, 193.
74 P.-Y. Chiou, Z. Chang and M. C. Wu, *J. Microelectromech. Syst.*, 2008, **17**, 133–138.
75 P. Y. Chiou, Z. Chang and M. C. Wu, presented in part at the 2003 12th International Conference on Solid-State Sensors, Actuators and Microsystems (Transducers), Boston, MA, USA, June, 2003.
76 P. Chiou, S.-Y. Park and M. C. Wu, *Appl. Phys. Lett.*, 2008, **93**, 221110.
77 T.-M. Yu, S.-M. Yang, C.-Y. Fu, M.-H. Liu, L. Hsu, H.-Y. Chang and C.-H. Liu, *Sens. Actuators, B*, 2013, **180**, 35–42.
78 S. N. Pei, J. K. Valley, S. L. Neale, A. Jamshidi, H.-Y. Hsu and M. C. Wu, presented in part at the 2010 IEEE 23rd international conference on micro electro mechanical systems (MEMS), Hong Kong, China, January, 2010.
79 H.-S. Chuang, A. Kumar and S. T. Wereley, *Appl. Phys. Lett.*, 2008, **93**, 064104.
80 S.-Y. Park, M. A. Teitell and E. P. Chiou, *Lab Chip*, 2010, **10**, 1655–1661.
81 E. Liu, C. Wang, H. Zheng, S. Song, A. Riaud and J. Zhou, *Sens. Actuators, B*, 2022, **368**, 132231.
82 M. Abdelgawad, S. L. S. Freire, H. Yang and A. R. Wheeler, *Lab Chip*, 2008, **8**, 672–677.
83 Y. Wang and Y.-P. Zhao, *Soft Matter*, 2012, **8**, 2599.
84 H. You and A. Steckl, *J. Adhes. Sci. Technol.*, 2012, **26**, 1931–1939.

85 J. B. Chae, S. J. Lee, J. Yang and S. K. Chung, *Sens. Actuators, A*, 2015, **234**, 331–338.
86 D. J. Preston, A. Anders, B. Barabadi, E. Tio, Y. Zhu, D. A. Dai and E. N. Wang, *Appl. Phys. Lett.*, 2016, **109**, 244102.
87 T.-C. Chu and Y.-W. Lu, *Micromachines*, 2021, **12**, 1385.
88 X. Min and W. S. Kim, *Langmuir*, 2020, **36**, 14841–14848.
89 S. Jun Lee, S. Lee and K. Hyoung Kang, *Appl. Phys. Lett.*, 2012, **100**, 081604.
90 F. Lapierre, Y. Coffinier, R. Boukherroub and V. Thomy, *Langmuir*, 2013, **29**, 13346–13351.
91 A. Merdasi, A. Moosavi and M. Shafii, *Mater. Res. Express*, 2019, **6**, 086333.
92 K. Takeda, A. Nakajima, K. Hashimoto and T. Watanabe, *Surf. Sci.*, 2002, **519**, L589–L592.
93 S.-K. Fan, H. Yang and W. Hsu, *Lab Chip*, 2011, **11**, 343–347.
94 H. Yang, W. Hsu and S.-K. Fan, presented in part at the *2008 IEEE 21st international conference on micro electro mechanical systems (MEMS)*, Tucson, AZ, USA, 2008.
95 C. Clement, D. Jiang, S. K. Thio and S.-Y. Park, *Materials*, 2017, **10**, 41.
96 H. Li, J. Cui, Z. Yan, M. Jin, Y. Zheng, G. Zhou and L. Shui, *Results Phys.*, 2021, **31**, 105042.
97 C. Li and H. Jiang, *Micromachines*, 2014, **5**, 432–441.
98 J. Ramanujam and A. Verma, *Mater. Express*, 2012, **2**, 177–196.
99 C.-H. Lee, A. Sazonov and A. Nathan, *Appl. Phys. Lett.*, 2005, **86**, 222106.
100 Z. Shen, T. Masuda, H. Takagishi, K. Ohdaira and T. Shimoda, *Chem. Commun.*, 2015, **51**, 4417–4420.
101 J. Joseph, S. G. Singh and S. R. K. Vanjari, *Mater. Lett.*, 2017, **197**, 52–55.
102 V. Zardetto, T. M. Brown, A. Reale and A. D. Carlo, *J. Polym. Sci., Part B: Polym. Phys.*, 2011, **49**, 638–648.
103 H.-j. Ni, J.-g. Liu, Z.-h. Wang and S.-y. Yang, *J. Ind. Eng. Chem.*, 2015, **28**, 16–27.
104 A. Uddin and X. Yang, *J. Nanosci. Nanotechnol.*, 2014, **14**, 1099–1119.
105 J. A. Bartelt, Z. M. Beiley, E. T. Hoke, W. R. Mateker, J. D. Douglas, B. A. Collins, J. R. Tumbleston, K. R. Graham, A. Amassian and H. Ade, *Adv. Energy Mater.*, 2013, **3**, 364–374.
106 Z. Tang, W. Tress and O. Inganäs, *Mater. Today*, 2014, **17**, 389–396.
107 S. K. Thio, S. Bae and S.-Y. Park, *Sens. Actuators, B*, 2020, **308**, 127704.
108 J. Yguerabide and E. E. Yguerabide, *Anal. Biochem.*, 1998, **262**, 157–176.
109 K. Aslan, J. R. Lakowicz and C. D. Geddes, *Curr. Opin. Chem. Biol.*, 2005, **9**, 538–544.
110 S. K. Thio and S.-Y. Park, *Micromachines*, 2022, **13**, 112.
111 M. Bai, Q. Zheng, Y. Tian, Z. Zhang, C. Chen, C. Cheng and X. Meng, *Water Res.*, 2016, **96**, 217–224.
112 C. Ng, T.-H. Le, S. G. Goh, L. Liang, Y. Kim, J. B. Rose and K. G. Yew-Hoong, *PLoS One*, 2015, **10**, e0143123.
113 O. Bastidas, *Technical Note-Neubauer Chamber Cell Counting*, 2013, pp. 1–6.
114 G. Bakalar, *SpringerPlus*, 2014, **3**, 1–8.
115 S. Lee, V. S. L. Khoo, C. A. D. Medriano, T. Lee, S.-Y. Park and S. Bae, *Water Res.*, 2019, **160**, 371–379.
116 N. A. Switz, M. V. D'Ambrosio and D. A. Fletcher, *PLoS One*, 2014, **9**, e95330.
117 S. Lee, S. Thio, S.-Y. Park and S. Bae, *Harmful Algae*, 2019, **88**, 101638.
118 S. K. Thio, S. Lee, S. Bae and S.-Y. Park, presented in part at the 2018 International Conference on Optical MEMS and Nanophotonics (OMN), Lausanne, Switzerland, July, 2018.

